Transformation Electromagnetics Based on the Schwarz-Christoffel Theorem for Conformal Array Design

M. Salucci, A. Polo, and G. Oliveri

Abstract

This work deals with the conformal transformation of linear phased arrays mounted on masts with arbitrary sections. Towards this goal, an innovative transformation electromagnetics (TE) methodology is introduced leveraging on the Schwarz-Christoffel (SC) theorem. Thanks to the SC-TE method it is possible to design meta-lenses with low anisotropy/complexity and doubly-connected contours, i.e., having internal forbidden regions/holes where the material properties cannot be arbitrarily changed. Some numerical results are shown in order to verify the effectiveness and the potential of the proposed design technique when dealing with conformal transformations with different degrees of deformation.

1 Definitions

- Maximum directivity

$$D_{max}(\theta,\varphi) = \frac{4\pi \max_{(\theta,\varphi)}\{|E(\theta,\varphi)|^2\}}{\int_0^{2\pi}\int_0^{\pi}|E(\theta,\varphi)|^2 \sin(\theta) d\theta d\varphi} \tag{1}$$

- Sidelobe level (SLL)

$$SLL = 20 \times log_{10}\left(\frac{\max\{F(\theta,\varphi)\}}{\max\{E(\theta,\varphi)\}}\right) \tag{2}$$

where $F(\theta,\varphi)$ is the $E(\theta,\varphi)$ secondary lobes

- Maximum lens permittivity

$$\max\{\underline{\underline{\varepsilon}}\} = \max_{\underline{r}\in\Omega}\{\varepsilon_{pq}(\underline{r});\ p,q\ \in\{1,2,3\}\} \tag{3}$$

- Minimum lens permittivity

$$\min\{\underline{\underline{\varepsilon}}\} = \min_{\underline{r}\in\Omega}\{\varepsilon_{pq}(\underline{r});\ p,q\ \in\{1,2,3\}\} \tag{4}$$

- Average fractional anisotropy

$$\alpha_F = \frac{1}{area(\Omega)}\int_{\underline{r}\in\Omega}\sqrt{\frac{3\sum_{i=1}^{3}[\sigma_i(\underline{r})-\sigma_{ave}(\underline{r})]^2}{2\sum_{i=1}^{3}[\sigma_i(\underline{r})]^2}}d\underline{r} \tag{5}$$

- Average relative anisotropy

$$\alpha_R = \frac{1}{area(\Omega)}\int_{\underline{r}\in\Omega}\sqrt{\frac{\sum_{i=1}^{3}[\sigma_i(\underline{r})-\sigma_{ave}(\underline{r})]^2}{3\sigma_{ave}(\underline{r})}}d\underline{r} \tag{6}$$

where

  - $\sigma_i(\underline{r}),\ i=1,...,3$ are the eigenvalues of the permittivity tensor $\underline{\underline{\varepsilon}}(\underline{r})$;
  - $\sigma_{ave}(\underline{r}) = \frac{\sum_{i=1}^{3}\sigma_i(\underline{r})}{3}$ is the average of the eigenvalues;
  - Ω is the space region that defines the lens

- Far-Field Matching Error

$$\xi = \frac{\sum_{u=1}^{U}\sum_{v=1,\ (u,v)\notin\Omega}^{V}|E_{est}(\theta_u,\varphi_v)-E_{ref}(\theta_u,\varphi_v)|^2}{\sum_{u=1}^{U}\sum_{v=1,\ (u,v)\notin\Omega}^{V}|E_{ref}(\theta_u,\varphi_v)|^2} \tag{7}$$

- Near-Field Matching Error

$$\chi = \frac{\sum_{u=1}^{U}\sum_{v=1,\ (u,v)\notin\Omega}^{V}|E_{est}(x_u,y_v)-E_{ref}(x_u,y_v)|^2}{\sum_{u=1}^{U}\sum_{v=1,\ (u,v)\notin\Omega}^{V}|E_{ref}(x_u,y_v)|^2} \tag{8}$$

2 Numerical Assessment

2.1 Analysis Vs. the Deformation Degree

In this analysis different degrees of deformation will be analyzed. The internal boundary of the lens (a circular shape) is described by the ellipse equation:

$$\frac{x^2}{a^2} + \frac{y^2}{b^2} = 1 \tag{9}$$

where $a = 1.2$ $[\lambda]$ is fixed while b is a value that describes the degree of deformation defined as

$$\Psi_i = 100 - \left((b_i - \min\{\underline{b}\}) \times \frac{100}{(\max\{\underline{b}\} - \min\{\underline{b}\})} \right) \quad \text{for } \underline{b} = \{b_1, ..., b_I\};\ i = 1, ..., I \tag{10}$$

where I is the number of deformation cases. The following deformation cases will be considered for $\underline{b} = \{0.1,\ 0.2,\ 0.4,\ 0.6,\ 0.8,\ 1.0,\ 1.$

- $\Psi = 0\% \rightarrow b = 1.2$
- $\Psi = 18\% \approx 20\% \rightarrow b = 1.0$
- $\Psi = 36\% \approx 40\% \rightarrow b = 0.8$
- $\Psi = 54\% \approx 50\% \rightarrow b = 0.6$
- $\Psi = 72\% \approx 70\% \rightarrow b = 0.4$
- $\Psi = 90\% \rightarrow b = 0.2$
- $\Psi = 100\% \rightarrow b = 0.1$

The target of this analysis is to analyze the behaviour of the near-field and far-field pattern in function of the deformation degree considering the following parameters:

- Maximum Directivity [dB];
- Side-Lobe Level (SLL) [dB];
- Half-Power Beamwidth (HPBW) [deg];
- First-Null Beamwidth (FNBW) [deg];
- Field Matching Error in far-field, ξ, and in near-field, χ;

2.1.1 Parameters

- Array:
  - Number of elements: $N = 6$
  - Radius of circular array: $r_{array} = 1.45\ [\lambda]$
  - Elements spacing: $d \simeq 0.52\ [\lambda]$
- Schwarz-Cristoffel Transformation:
  - Virtual Region
    - Virtual ground plane radius: $r_{virt-gnd} = 1.2\ [\lambda]$
    - Distance from the ground plane: $\delta = r_{array} - r_{virt-gnd} = \frac{\lambda}{4}$
    - Virtual permittivity: $\varepsilon = 1$
    - Virtual permeability: $\mu = 1$
  - Physical Region
    - External radius: $L_{ext} = 5\ [\lambda]$
    - External Lens boundary : $\partial\Omega_{ext} = \left\{(x, y) \in \mathbb{R} \mid \sqrt{x^2 + y^2} = L_{ext}\right\}\ [\lambda]$
    - Internal Lens boundary:

$$\partial\Omega_{int} \quad = \quad \left\{(x,\, y) \in \mathbb{R} \wedge\ a = 1.2\ \wedge\ b = \{0.1,\, 0.2,\, 0.4,\, 0.6,\, 0.8,\, 1.0,\, 1.2\} \middle| \frac{x^2}{a^2} + \frac{y^2}{b^2} = 1\right\}\ [\lambda]$$

    - Number of points defining the external boundary: $n_{ext} = 25$
    - Number of points defining the internal boundary: $n_{int} = 15$
- SCTO parameters
  - Error tolerance: 10^{-10}
  - Number of Gauss-Jacobi points (nodes): 10
  - Discretization in virtual grid (outer boundary): $\Delta = 0.2\ [\lambda]$
- Simulation Environment
  - Working frequency: $f_w = 300\ [MHz]$
  - Simulation region: $\begin{cases} x \in [-20,\, 20]\ [\lambda] \\ y \in [-20,\, 20]\ [\lambda] \end{cases}$
  - Near-Field computation: $\begin{cases} x \in [-20,\, 20]\ [\lambda] \\ y \in [-20,\, 20]\ [\lambda] \end{cases}$
  - Far-Field computation: $\begin{cases} \theta = \frac{\pi}{2}\ [rad] \\ \varphi \in [0,\, \pi]\ [rad] \end{cases}$

– Mesh settings

  * Size: $size_{mesh} \in [5 \times 10^{-4}, 0.2]$
  * Maximum growth rate: 1.3
  * Curvature factor: 0.3
  * Narrow region resolution: 1

– Simulation region layer thickness: 1

2.1.2 Results

Deformation $\Psi = 0\%$

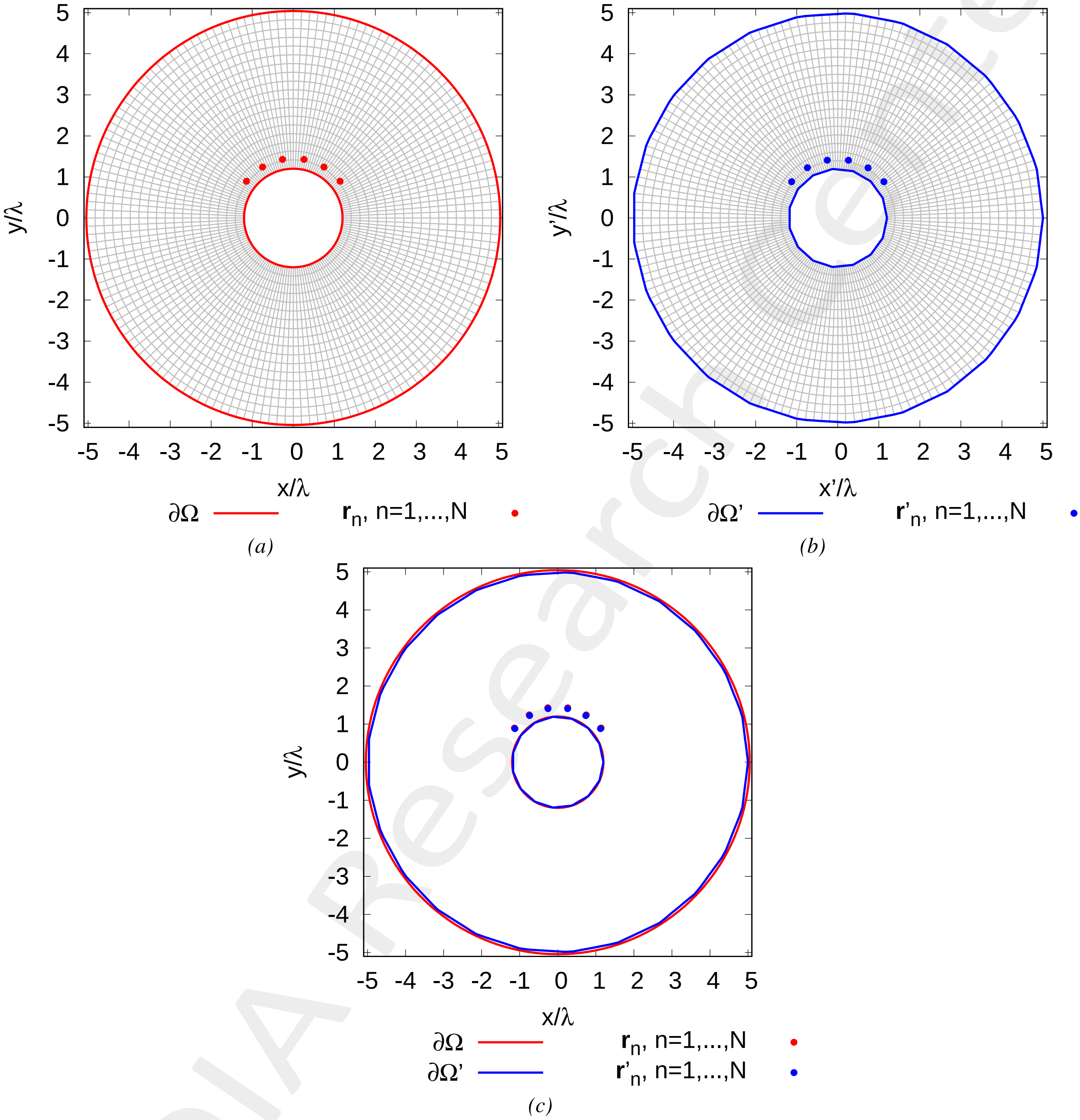

Figure 1: *(a)* Virtual, *(b)* Physical geometries and *(c)* the comparison

Physical Permittivity Properties	
Average fractional anisotropy α_F	0.0239606
Average relative anisotropy α_R	0.0198299

Table I: Average fractional anisotropy α_F and average relative anisotropy α_R

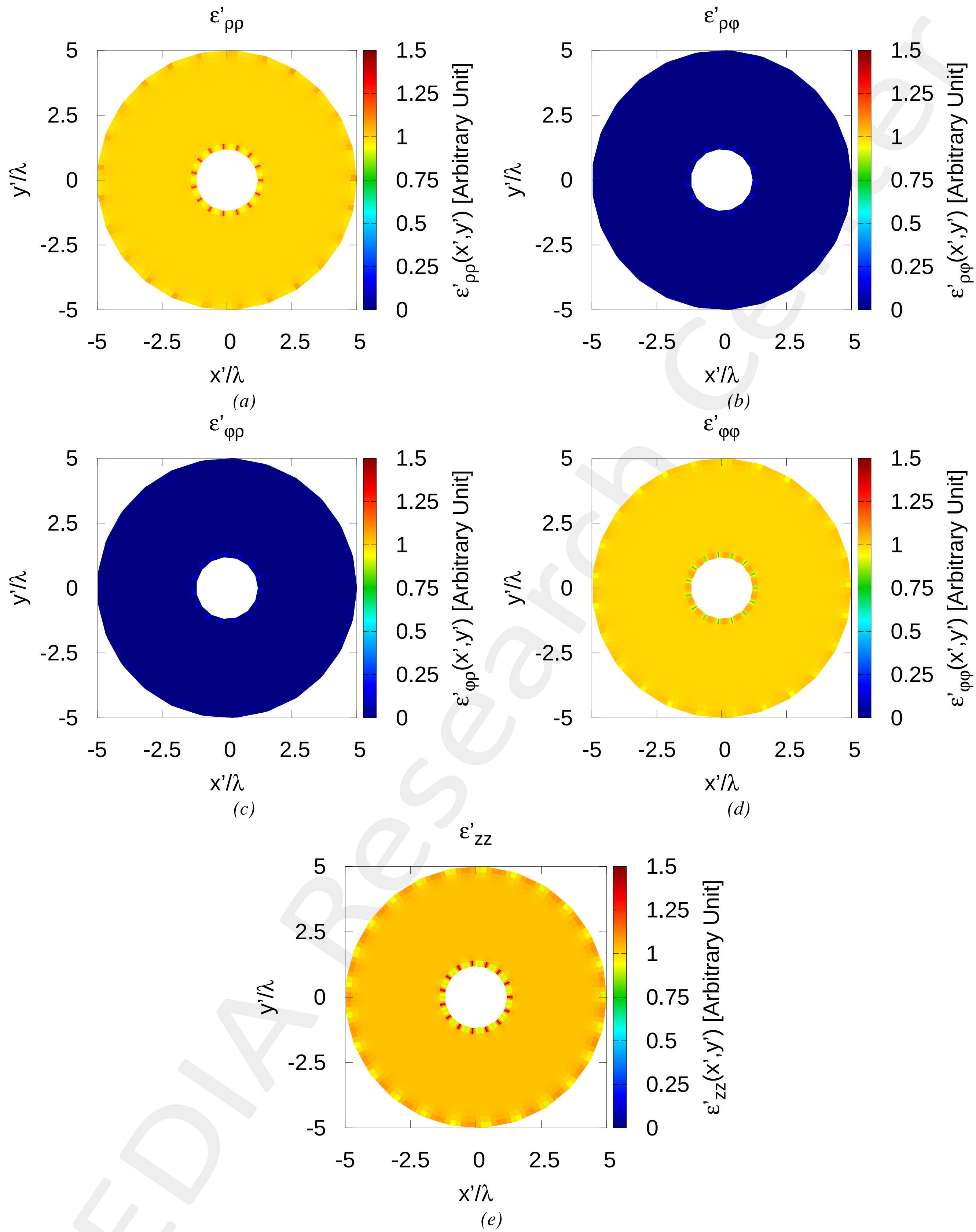

Figure 2: Tensor permittivity values for *(a)* $\varepsilon'_{\rho\rho}$, *(b)* $\varepsilon'_{\rho\varphi}$, *(c)* $\varepsilon'_{\varphi\rho}$, *(d)* $\varepsilon'_{\varphi\varphi}$, *(e)* ε'_{zz}

mimimum/maximum	min	max
$\varepsilon'_{\rho\rho}$	9.4559×10^{-1}	1.2833
$\varepsilon'_{\rho\varphi}$	-1.71×10^{-1}	1.1488×10^{-1}
$\varepsilon'_{\varphi\rho}$	-1.71×10^{-1}	1.1488×10^{-1}
$\varepsilon'_{\varphi\varphi}$	7.7928×10^{-1}	1.057
ε'_{zz}	9.0267×10^{-1}	1.4840
global minimum/maximum	$\min\{\underline{\underline{\varepsilon}}'\} = -0.17$	$\max\{\underline{\underline{\varepsilon}}'\} = 1.48$

Table II: Statistics about the permittivity lens reporting minimum and maximum value for every component of $\underline{\underline{\varepsilon}}'$, global minimum $\min\{\underline{\underline{\varepsilon}}'\}$ and global maximum $\max\{\underline{\underline{\varepsilon}}'\}$

	Virtual	Physical	Physical (No Lens)
SLL [dB]	-12.40	-12.01	-12.30
Directivity [dB]	8.82	8.76	8.75
FNBW [deg]	47.09	47.36	47.45
HPBW [deg]	20.54	20.59	20.80
Field Matching Error ξ (7)	$\times$	2.6234×10^{-3}	2.7606×10^{-4}
Field Matching Error χ (8)	$\times$	2.2669×10^{-1}	7.6591×10^{-3}

Table III: Pattern values for the virtual, physical and physical (no lens) cases

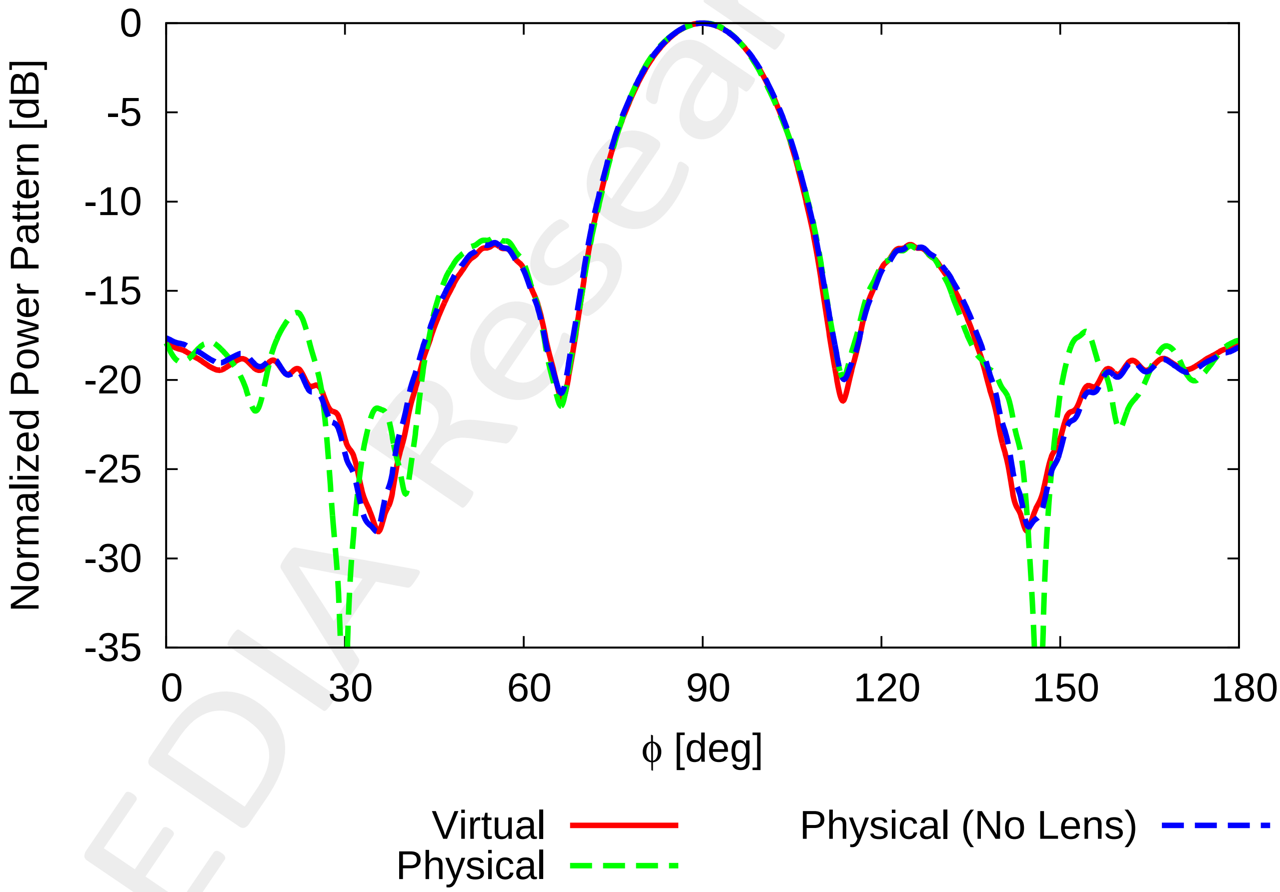

Figure 3: Far-Field Pattern for $\theta = 90$ [deg] and $\varphi \in [0, 180]$ [deg]

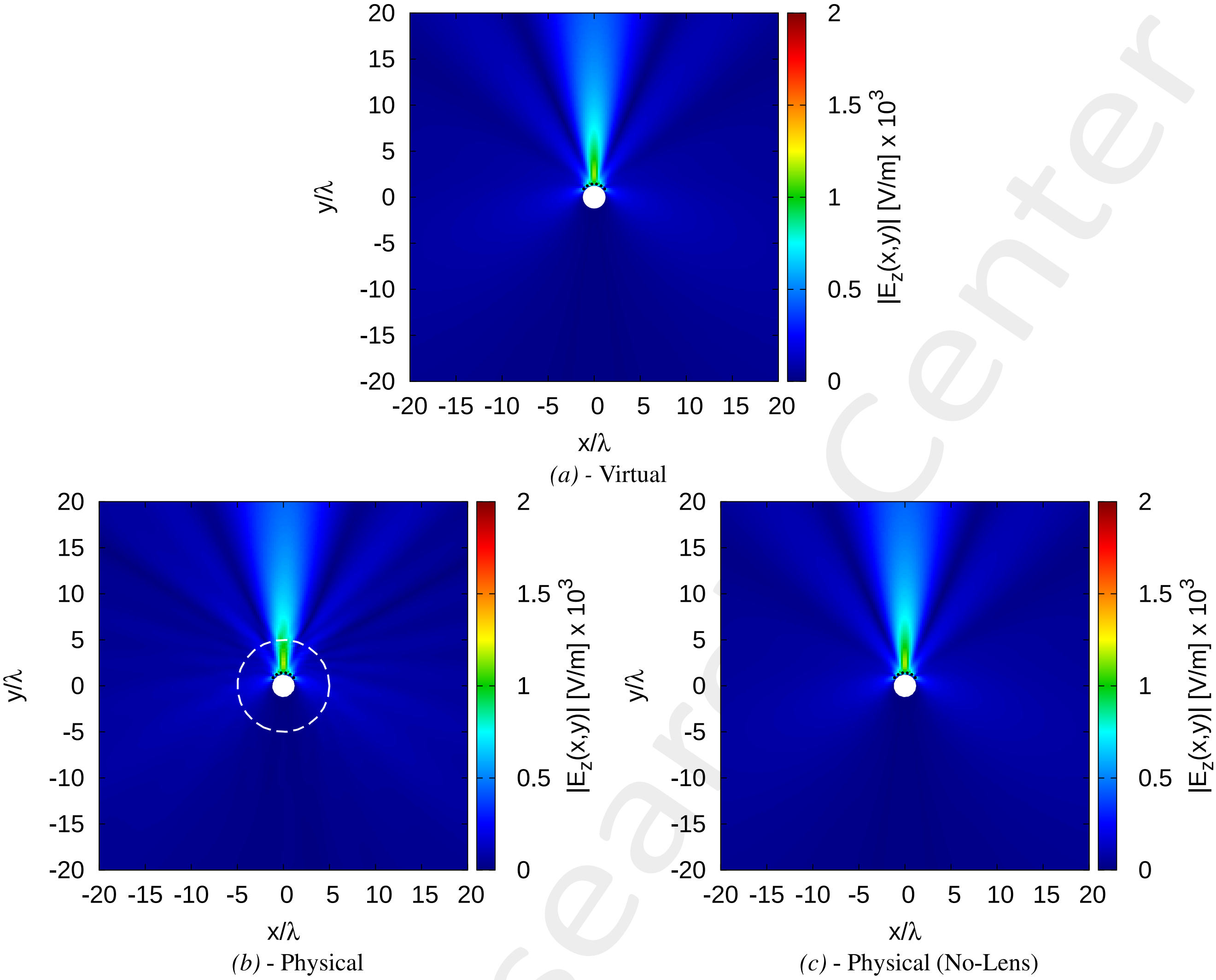

Figure 4: Near-Field pattern in the *(a)* virtual, *(b)* physical and *(c)* no-lens

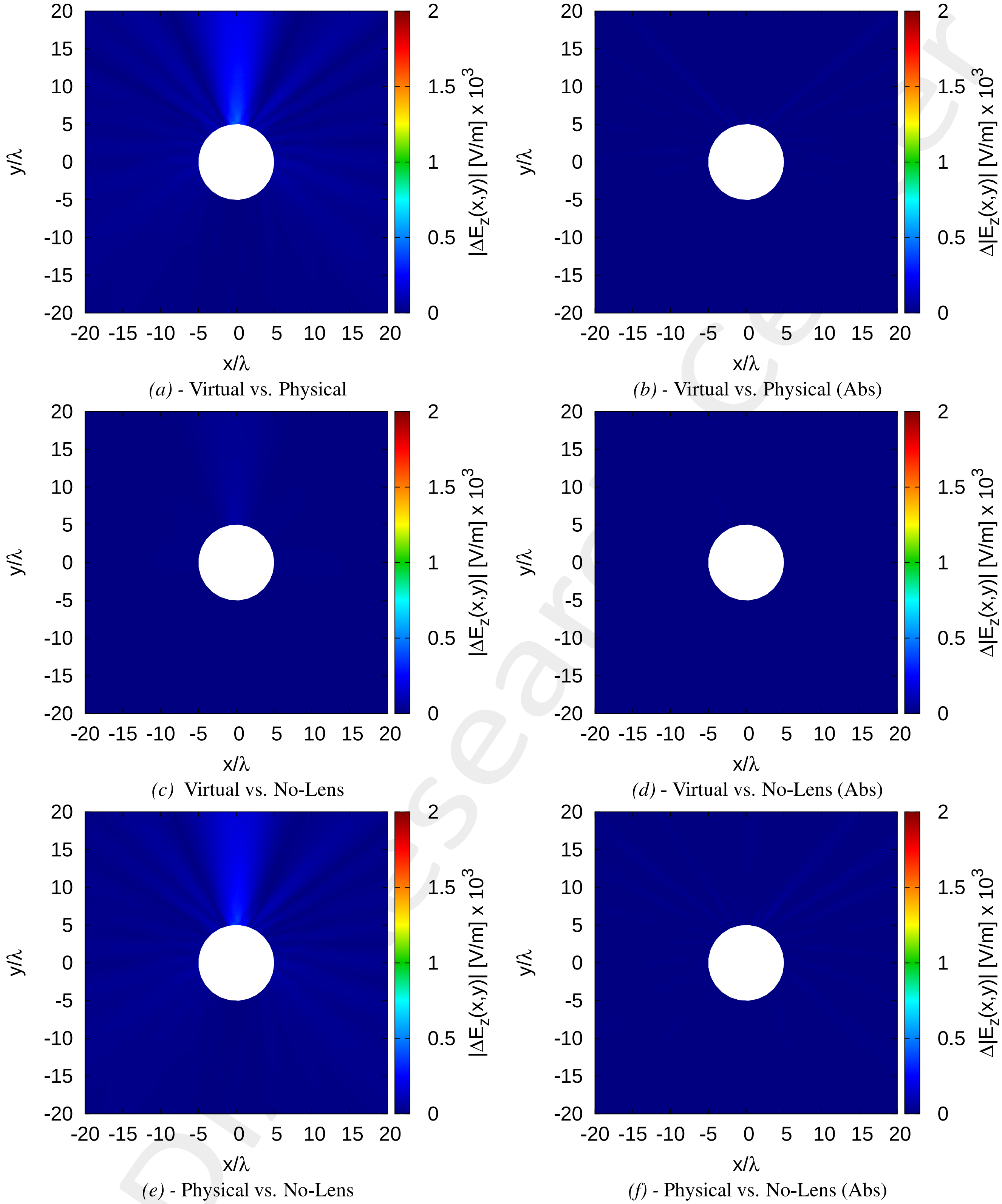

(a) - Virtual vs. Physical

(b) - Virtual vs. Physical (Abs)

(c) Virtual vs. No-Lens

(d) - Virtual vs. No-Lens (Abs)

(e) - Physical vs. No-Lens

(f) - Physical vs. No-Lens (Abs)

Figure 5: Near-Field difference pattern in the *(a)(b)* virtual vs. physical, *(c)(d)* virtual vs. no-lens and *(e)(f)* physical vs. no-lens. The difference pattern is computed for the *(a)(c)(e)* cases as $\left|\Delta E_z\right| \triangleq \left|E_z^{ref}(x,y) - E_z^{est}(x,y)\right|_{(x,y)\notin\Omega}$ while for the *(b)(d)(f)* cases as $\Delta\left|E_z\right| \triangleq \left[\left|E_z^{ref}(x,y)\right| - \left|E_z^{est}(x,y)\right|\right]_{(x,y)\notin\Omega}$

Deformation $\Psi = 20\%$

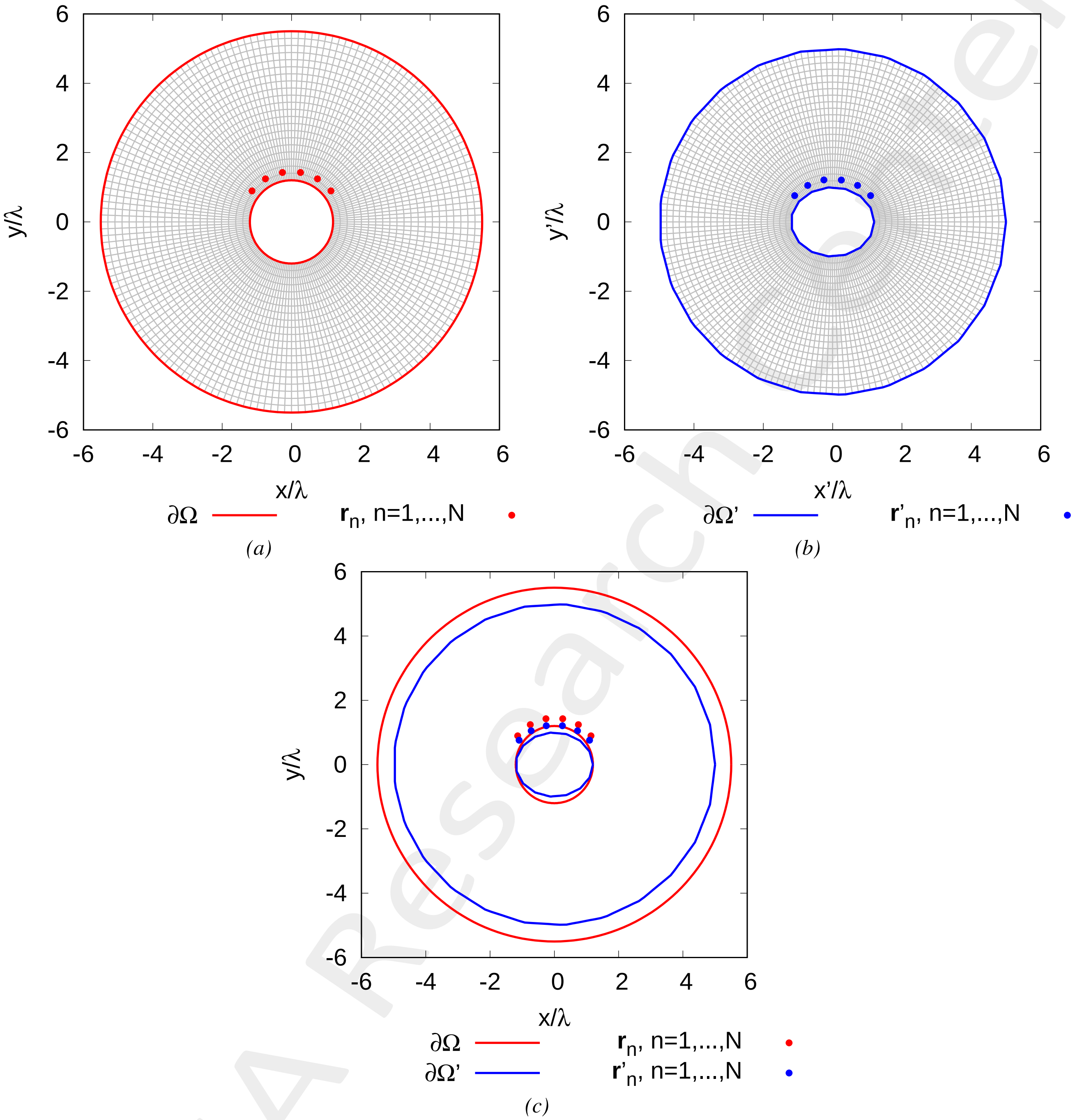

Figure 6: *(a)* Virtual, *(b)* Physical geometries and *(c)* the comparison

Physical Permittivity Properties	
Average fractional anisotropy α_F	0.122244
Average relative anisotropy α_R	0.104526

Table IV: Average fractional anisotropy α_F and average relative anisotropy α_R

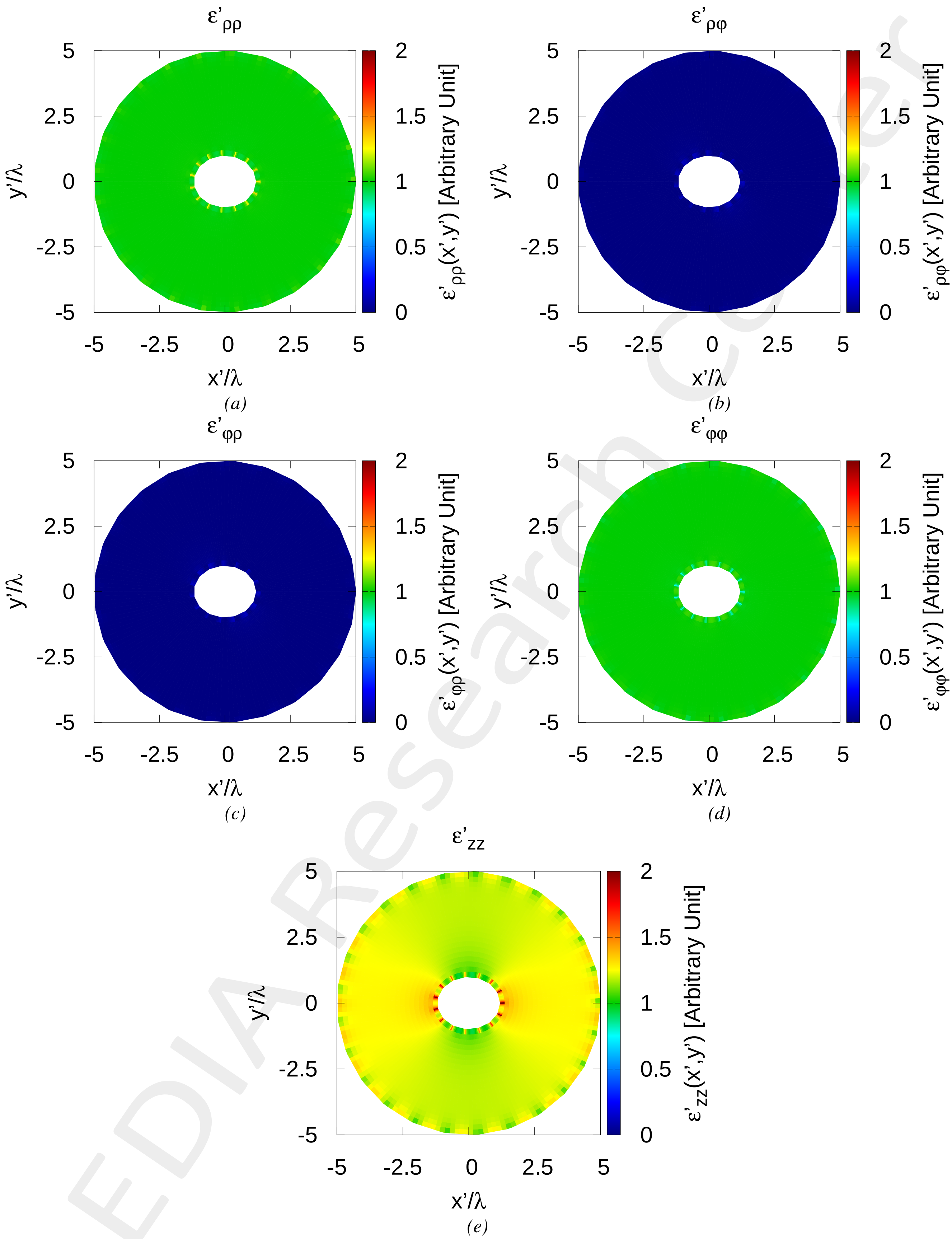

Figure 7: Tensor permittivity values for *(a)* $\varepsilon'_{\rho\rho}$, *(b)* $\varepsilon'_{\rho\varphi}$, *(c)* $\varepsilon'_{\varphi\rho}$, *(d)* $\varepsilon'_{\varphi\varphi}$, *(e)* ε'_{zz}

mimimum/maximum	min	max
$\varepsilon'_{\rho\rho}$	9.4362×10^{-1}	1.3599
$\varepsilon'_{\rho\varphi}$	-2.0015×10^{-1}	1.2539×10^{-1}
$\varepsilon'_{\varphi\rho}$	-2.0015×10^{-1}	1.2539×10^{-1}
$\varepsilon'_{\varphi\varphi}$	7.3642×10^{-1}	1.06
ε'_{zz}	9.3289×10^{-1}	2.2429
global minimum/maximum	$\min\{\underline{\underline{\varepsilon}}'\} = -0.20$	$\max\{\underline{\underline{\varepsilon}}'\} = 2.24$

Table V: Statistics about the permittivity lens reporting minimum and maximum value for every component of $\underline{\underline{\varepsilon}}'$, global minimum $\min\{\underline{\underline{\varepsilon}}'\}$ and global maximum $\max\{\underline{\underline{\varepsilon}}'\}$

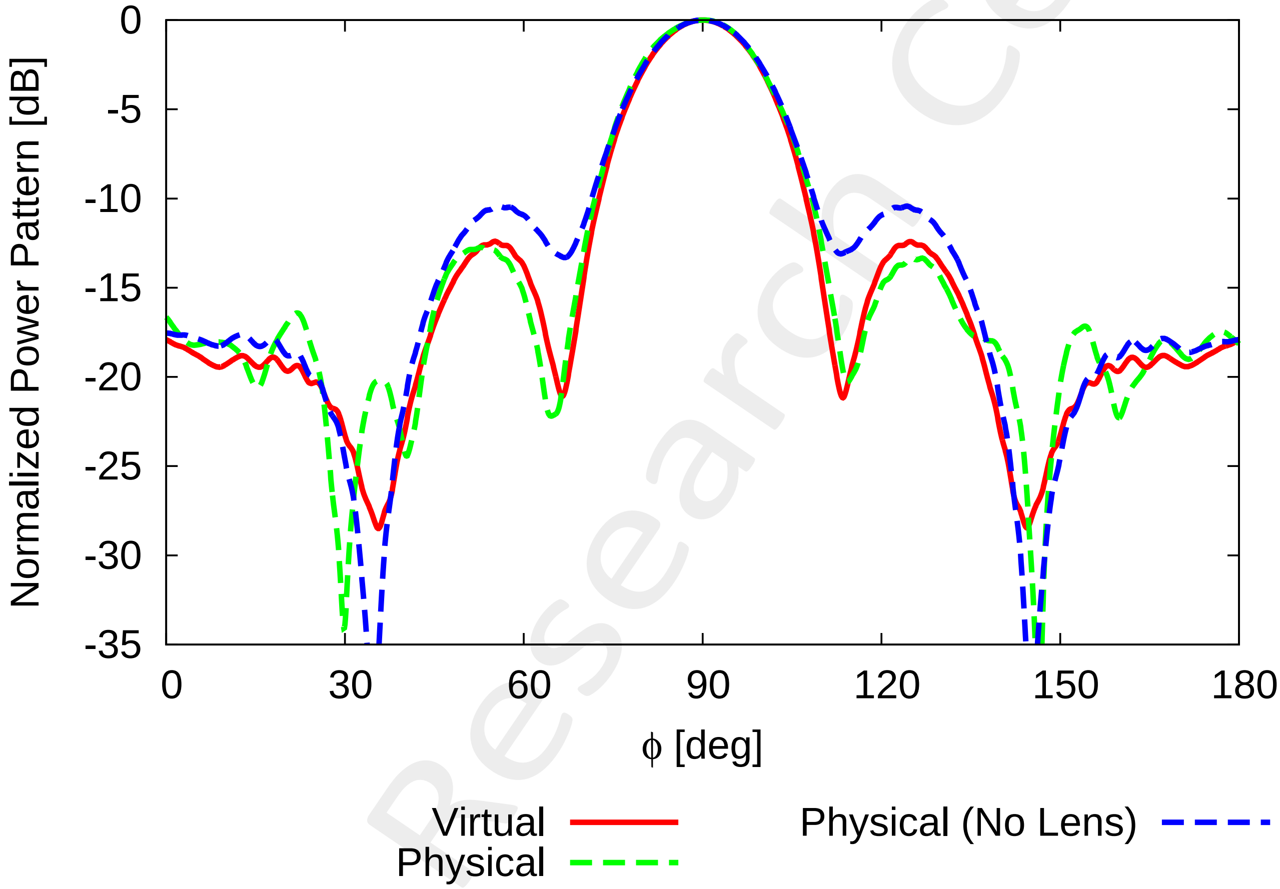

Figure 8: Far-Field Pattern for $\theta = 90$ [deg] and $\varphi \in [0, 180]$ [deg]

	Virtual	Physical	Physical (No Lens)
SLL [dB]	-12.40	-12.74	-10.41
Directivity [dB]	8.82	8.65	8.37
FNBW [deg]	47.09	49.70	46.28
HPBW [deg]	20.54	21.38	21.56
Field Matching Error ξ (7)	$\times$	5.2778×10^{-3}	1.2774×10^{-2}
Field Matching Error χ (8)	$\times$	4.0630	9.7519×10^{-1}

Table VI: Pattern values for the virtual, physical and physical (no lens) cases

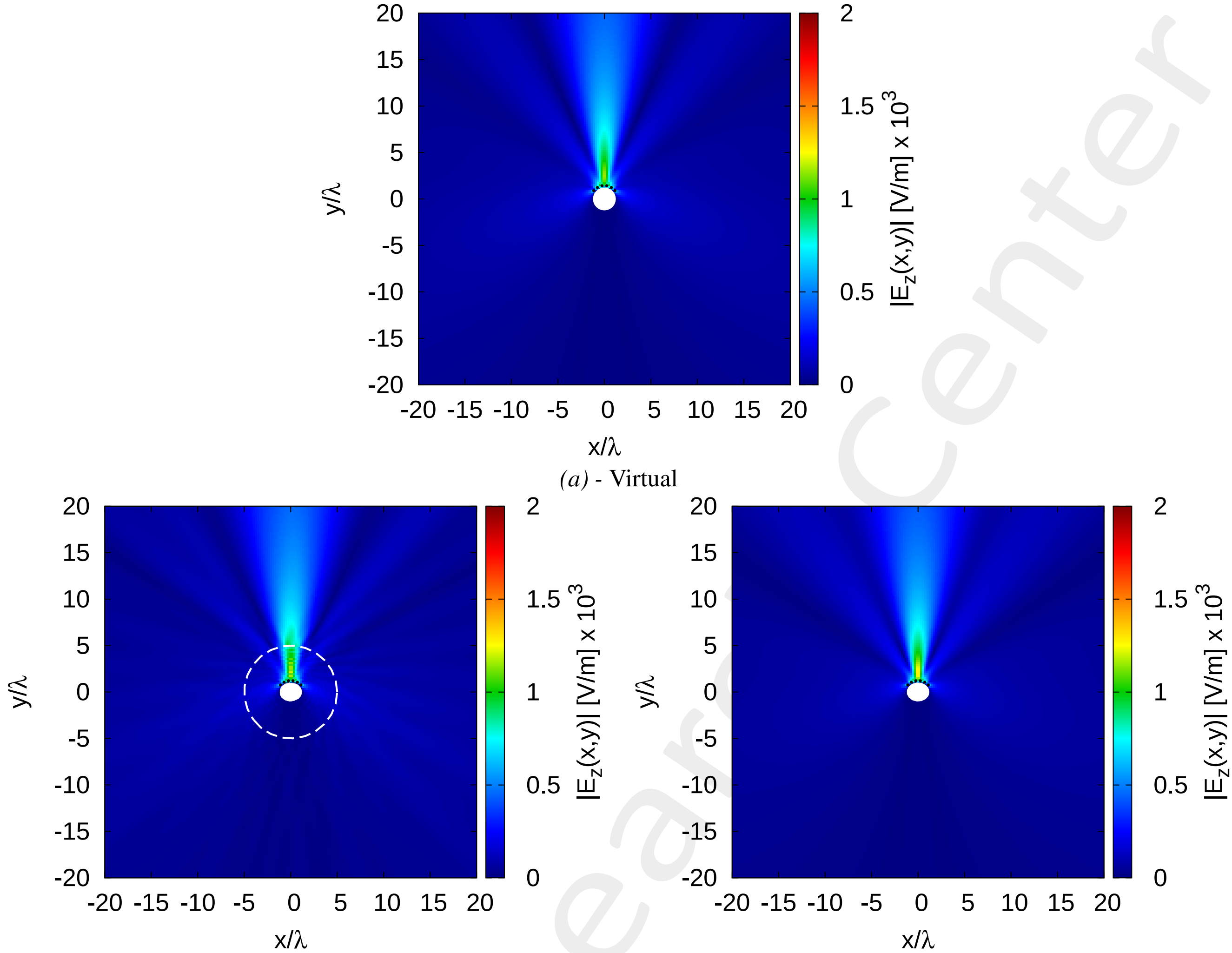

(a) - Virtual

(b) - Physical

(c) - Physical (No-Lens)

Figure 9: Near-Field pattern in the *(a)* virtual, *(b)* physical and *(c)* no-lens

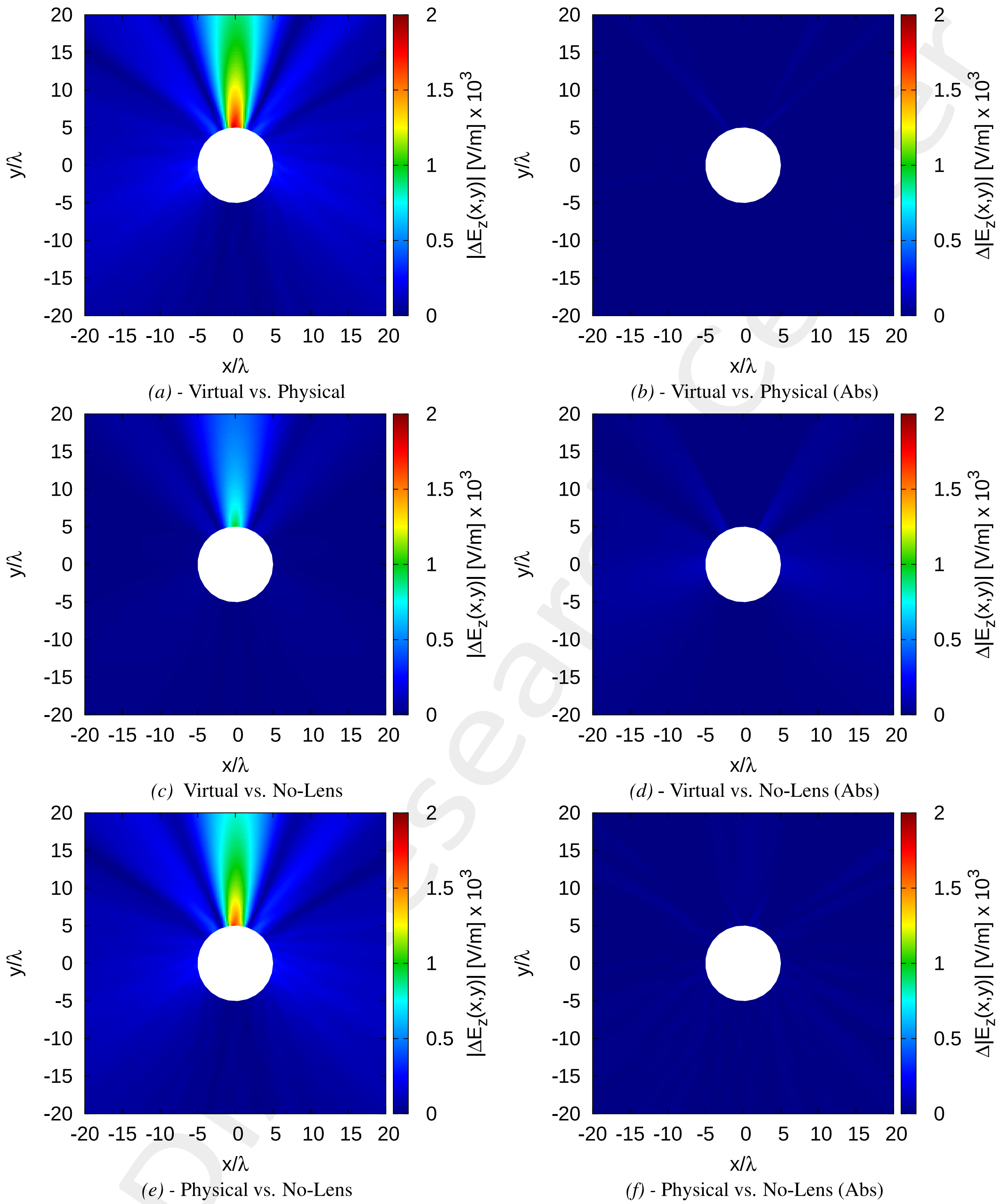

Figure 10: Near-Field difference pattern in the *(a)(b)* virtual vs. physical, *(c)(d)* virtual vs. no-lens and *(e)(f)* physical vs. no-lens. The difference pattern is computed for the *(a)(c)(e)* cases as $|\Delta E_z| \triangleq \left|E_z^{ref}(x,y) - E_z^{est}(x,y)\right|_{(x,y)\notin\Omega}$ while for the *(b)(d)(f)* cases as $\Delta|E_z| \triangleq \left[\left|E_z^{ref}(x,y)\right| - \left|E_z^{est}(x,y)\right|\right]_{(x,y)\notin\Omega}$

Deformation $\Psi = 40\%$

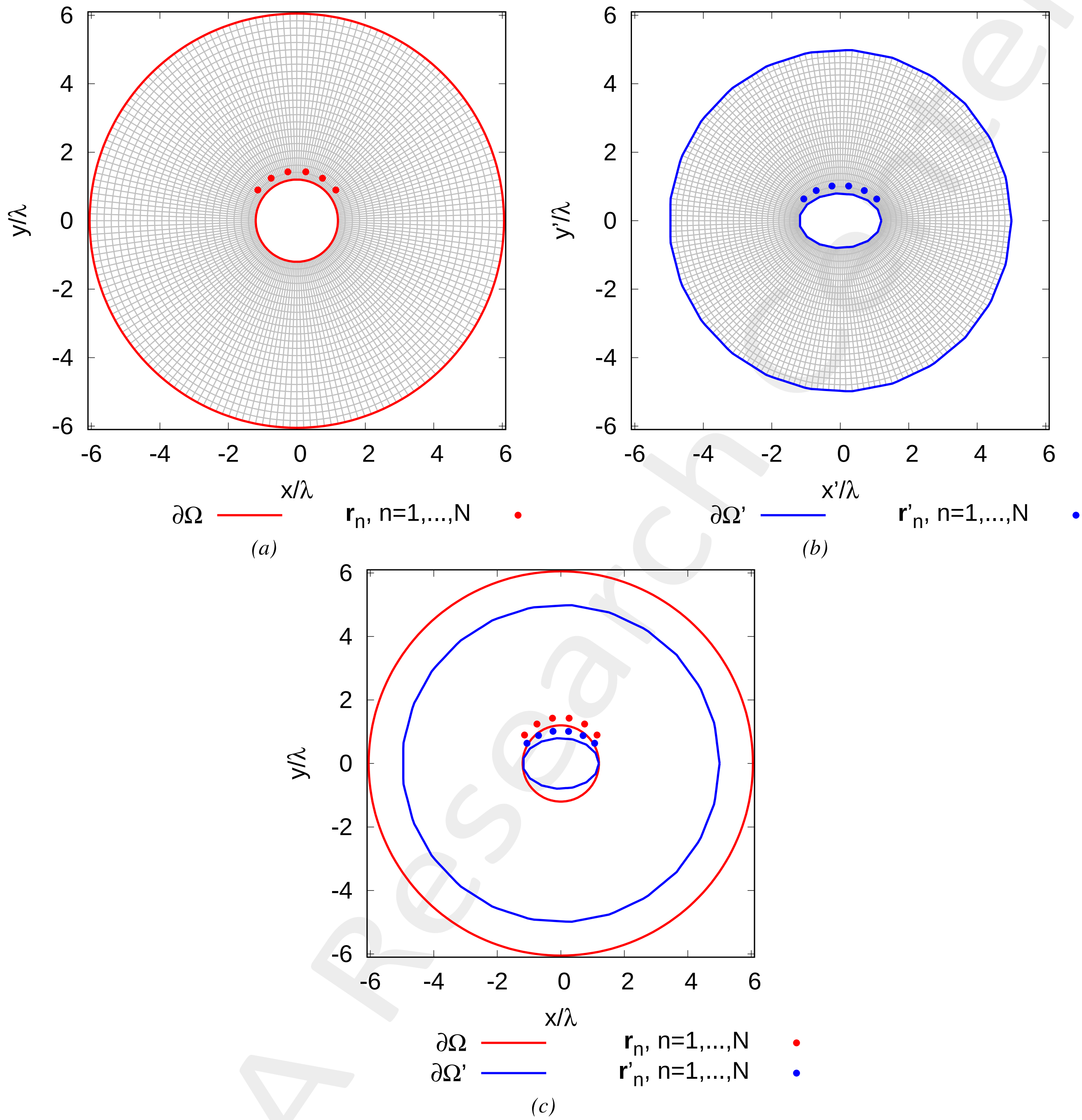

Figure 11: *(a)* Virtual, *(b)* Physical geometries and *(c)* the comparison

Physical Permittivity Properties	
Average fractional anisotropy α_F	0.236264
Average relative anisotropy α_R	0.213999

Table VII: Average fractional anisotropy α_F and average relative anisotropy α_R

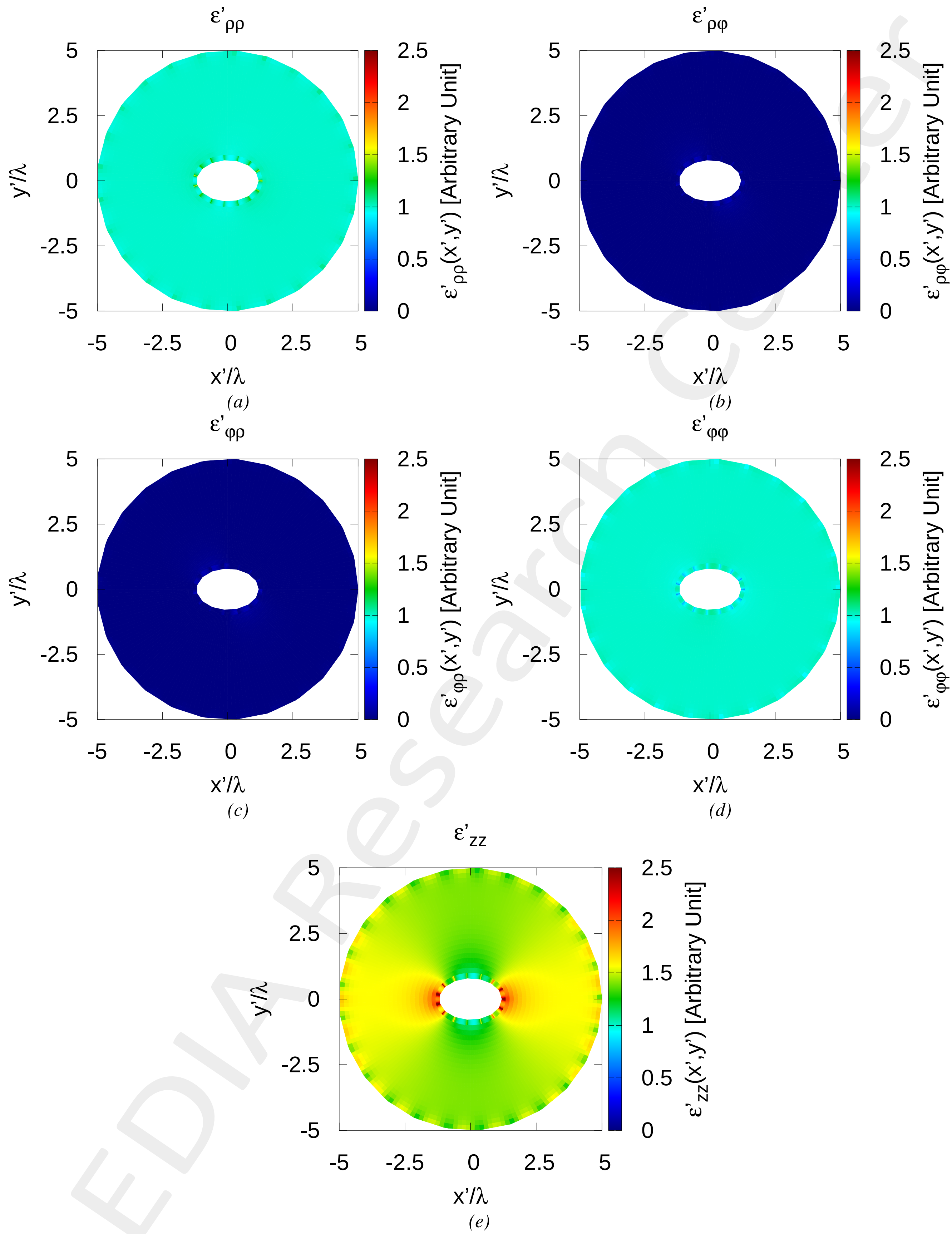

Figure 12: Tensor permittivity values for *(a)* $\varepsilon'_{\rho\rho}$, *(b)* $\varepsilon'_{\rho\varphi}$, *(c)* $\varepsilon'_{\varphi\rho}$, *(d)* $\varepsilon'_{\varphi\varphi}$, *(e)* ε'_{zz}

mimimum/maximum	min	max
$\varepsilon'_{\rho\rho}$	9.3972×10^{-1}	1.513
$\varepsilon'_{\rho\varphi}$	-2.4021×10^{-1}	1.6018×10^{-1}
$\varepsilon'_{\varphi\rho}$	-2.4021×10^{-1}	1.6018×10^{-1}
$\varepsilon'_{\varphi\varphi}$	6.6783×10^{-1}	1.0644
ε'_{zz}	9.6692×10^{-1}	3.6260
global minimum/maximum	$\min\{\underline{\underline{\varepsilon}}'\} = -0.24$	$\max\{\underline{\underline{\varepsilon}}'\} = 3.63$

Table VIII: Statistics about the permittivity lens reporting minimum and maximum value for every component of $\underline{\underline{\varepsilon}}'$, global minimum $\min\{\underline{\underline{\varepsilon}}'\}$ and global maximum $\max\{\underline{\underline{\varepsilon}}'\}$

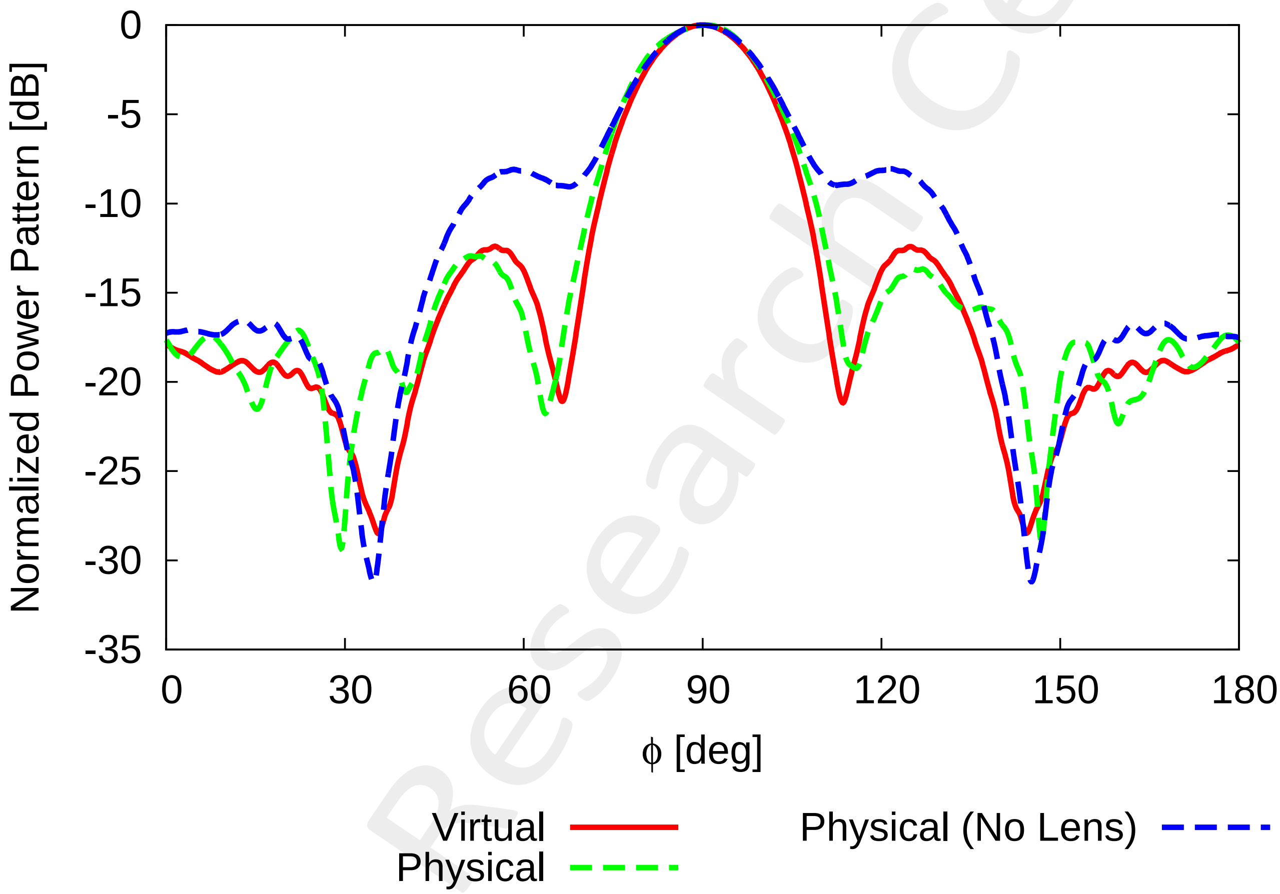

Figure 13: Far-Field Pattern for $\theta = 90$ [deg] and $\varphi \in [0, 180]$ [deg]

	Virtual	Physical	Physical (No Lens)
SLL [dB]	-12.40	-12.93	-8.05
Directivity [dB]	8.82	8.51	7.72
FNBW [deg]	47.09	52.13	44.84
HPBW [deg]	20.54	22.09	22.01
Field Matching Error ξ (7)	$\times$	1.1433×10^{-2}	5.299×10^{-2}
Field Matching Error χ (8)	$\times$	2.7822×10^{-1}	2.5870

Table IX: Pattern values for the virtual, physical and physical (no lens) cases

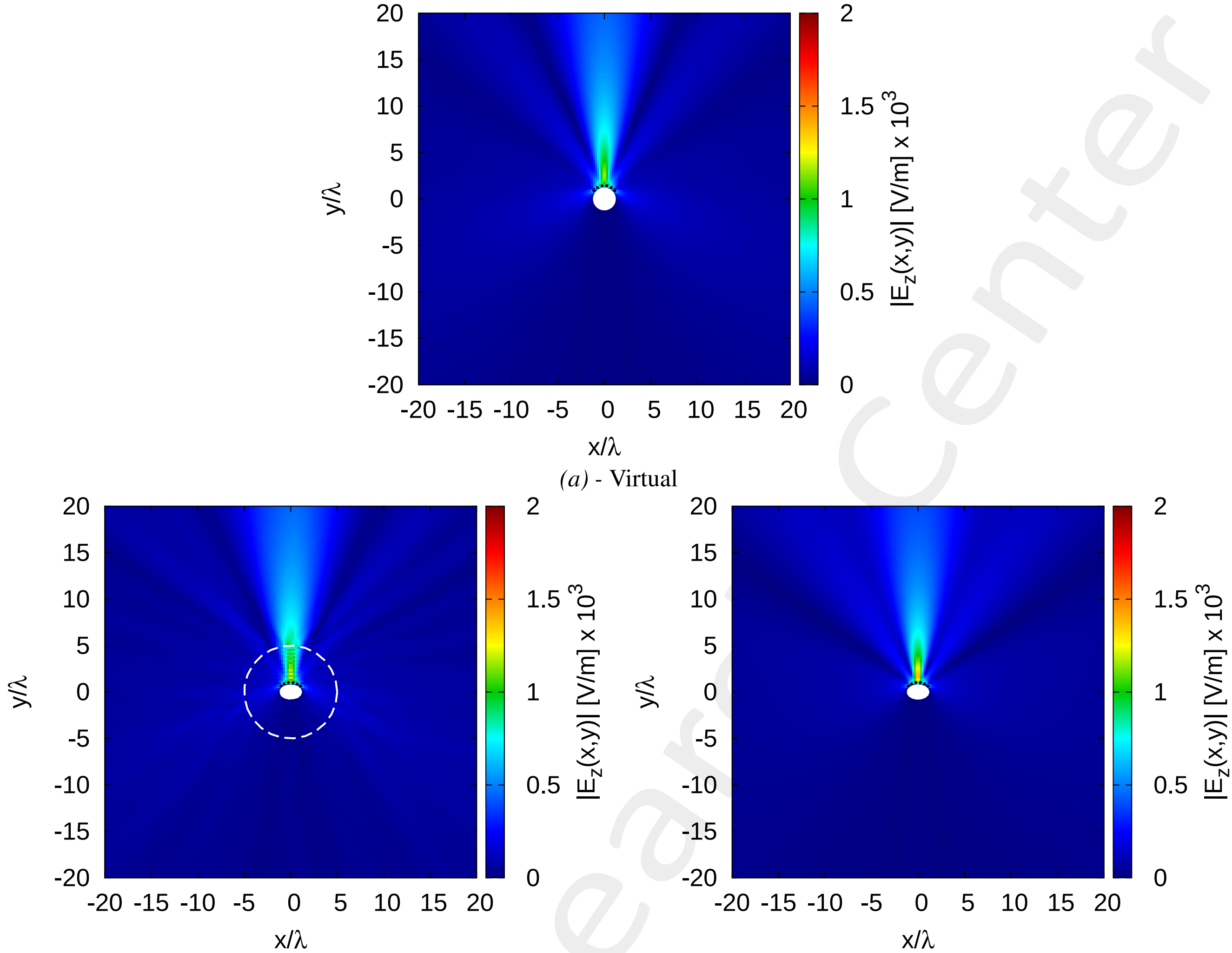

(a) - Virtual

(b) - Physical

(c) - Physical (No-Lens)

Figure 14: Near-Field pattern in the *(a)* virtual, *(b)* physical and *(c)* no-lens

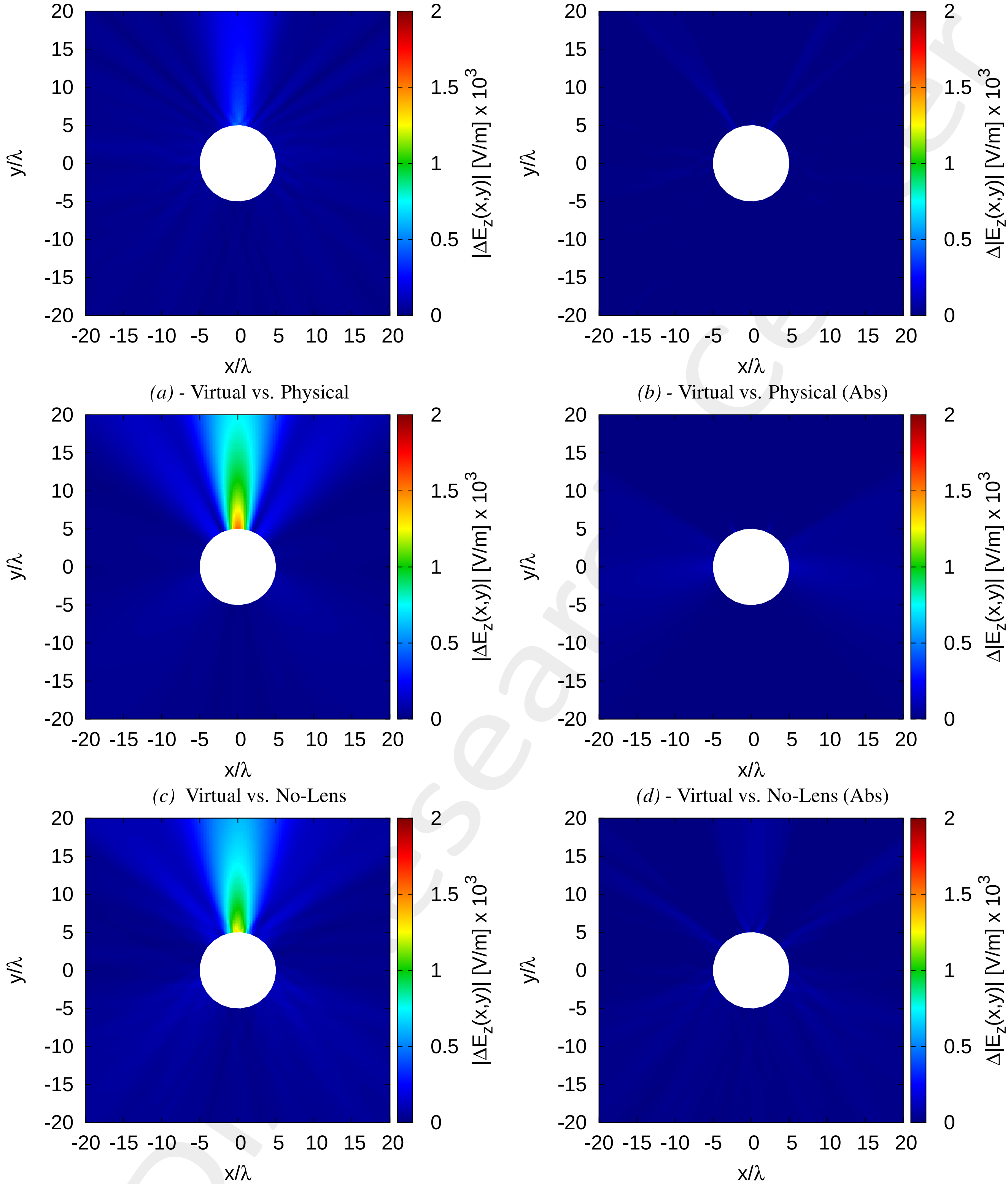

(a) - Virtual vs. Physical

(b) - Virtual vs. Physical (Abs)

(c) Virtual vs. No-Lens

(d) - Virtual vs. No-Lens (Abs)

(e) - Physical vs. No-Lens

(f) - Physical vs. No-Lens (Abs)

Figure 15: Near-Field difference pattern in the *(a)(b)* virtual vs. physical, *(c)(d)* virtual vs. no-lens and *(e)(f)* physical vs. no-lens. The difference pattern is computed for the *(a)(c)(e)* cases as $|\Delta E_z| \triangleq \left|E_z^{ref}(x,y) - E_z^{est}(x,y)\right|_{(x,y)\notin\Omega}$ while for the *(b)(d)(f)* cases as $\Delta|E_z| \triangleq \left[\left|E_z^{ref}(x,y)\right| - \left|E_z^{est}(x,y)\right|\right]_{(x,y)\notin\Omega}$

Deformation $\Psi = 50\%$

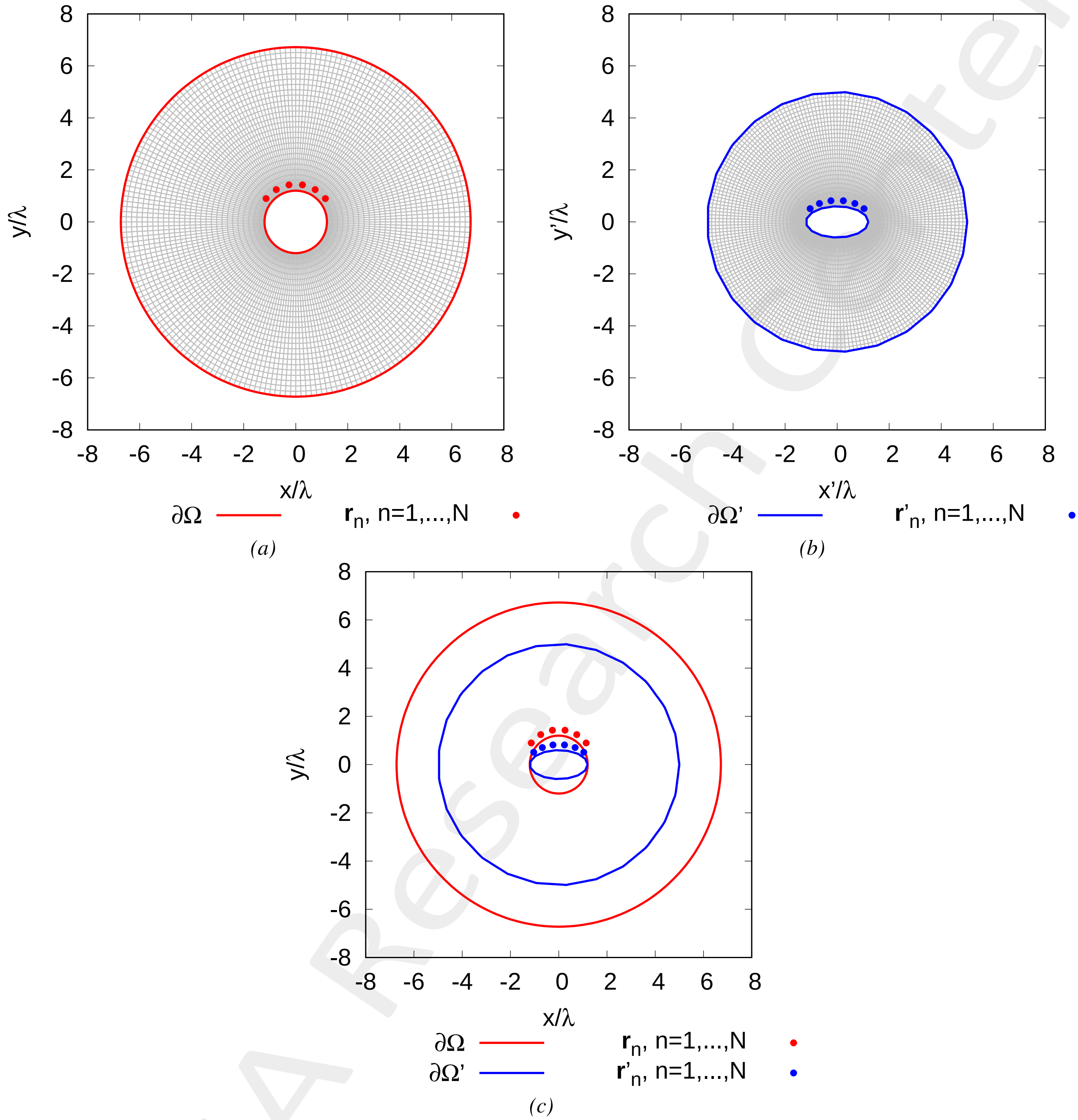

Figure 16: *(a)* Virtual, *(b)* Physical geometries and *(c)* the comparison

Physical Permittivity Properties	
Average fractional anisotropy α_F	0.357747
Average relative anisotropy α_R	0.351688

Table X: Average fractional anisotropy α_F and average relative anisotropy α_R

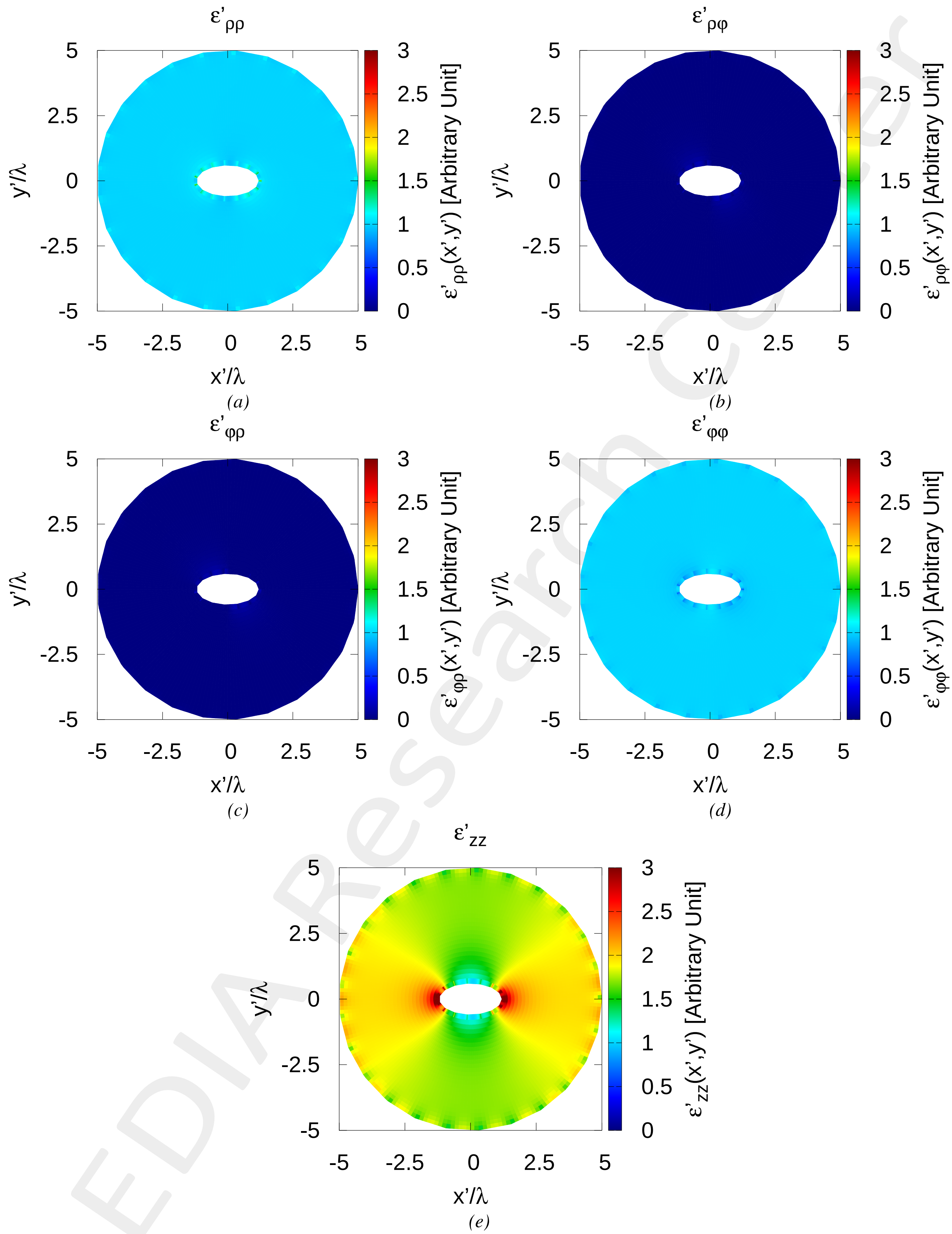

Figure 17: Tensor permittivity values for *(a)* $\varepsilon'_{\rho\rho}$, *(b)* $\varepsilon'_{\rho\varphi}$, *(c)* $\varepsilon'_{\varphi\rho}$, *(d)* $\varepsilon'_{\varphi\varphi}$, *(e)* ε'_{zz}

mimimum/maximum	min	max
$\varepsilon'_{\rho\rho}$	9.3681×10^{-1}	1.692
$\varepsilon'_{\rho\varphi}$	-3.5974×10^{-1}	2.07×10^{-1}
$\varepsilon'_{\varphi\rho}$	-9.5974×10^{-1}	2.07×10^{-1}
$\varepsilon'_{\varphi\varphi}$	6.091×10^{-1}	1.0676
ε'_{zz}	9.9981×10^{-1}	7.3668
global minimum/maximum	$\min\{\underline{\underline{\varepsilon}}'\} = -0.36$	$\max\{\underline{\underline{\varepsilon}}'\} = 7.37$

Table XI: Statistics about the permittivity lens reporting minimum and maximum value for every component of $\underline{\underline{\varepsilon}}'$, global minimum $\min\{\underline{\underline{\varepsilon}}'\}$ and global maximum $\max\{\underline{\underline{\varepsilon}}'\}$

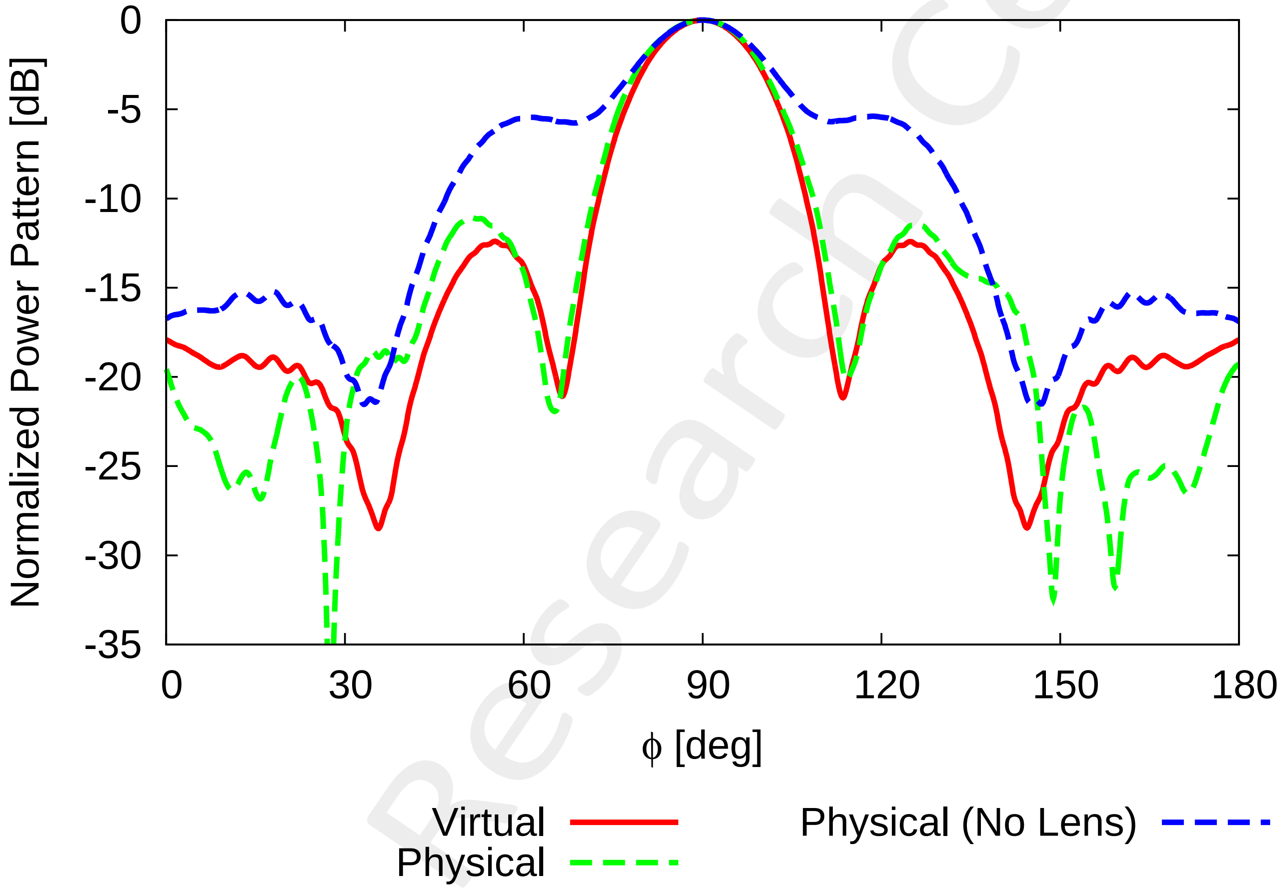

Figure 18: Far-Field Pattern for $\theta = 90$ [deg] and $\varphi \in [0, 180]$ [deg]

	Virtual	Physical	Physical (No Lens)
SLL [dB]	-12.40	-11.05	-5.39
Directivity [dB]	8.82	8.52	6.70
FNBW [deg]	47.09	48.98	43.04
HPBW [deg]	20.54	21.87	24.13
Field Matching Error ξ (7)	$\times$	1.5658×10^{-2}	1.2604×10^{-1}
Field Matching Error χ (8)	$\times$	1.9615	3.2102

Table XII: Pattern values for the virtual, physical and physical (no lens) cases

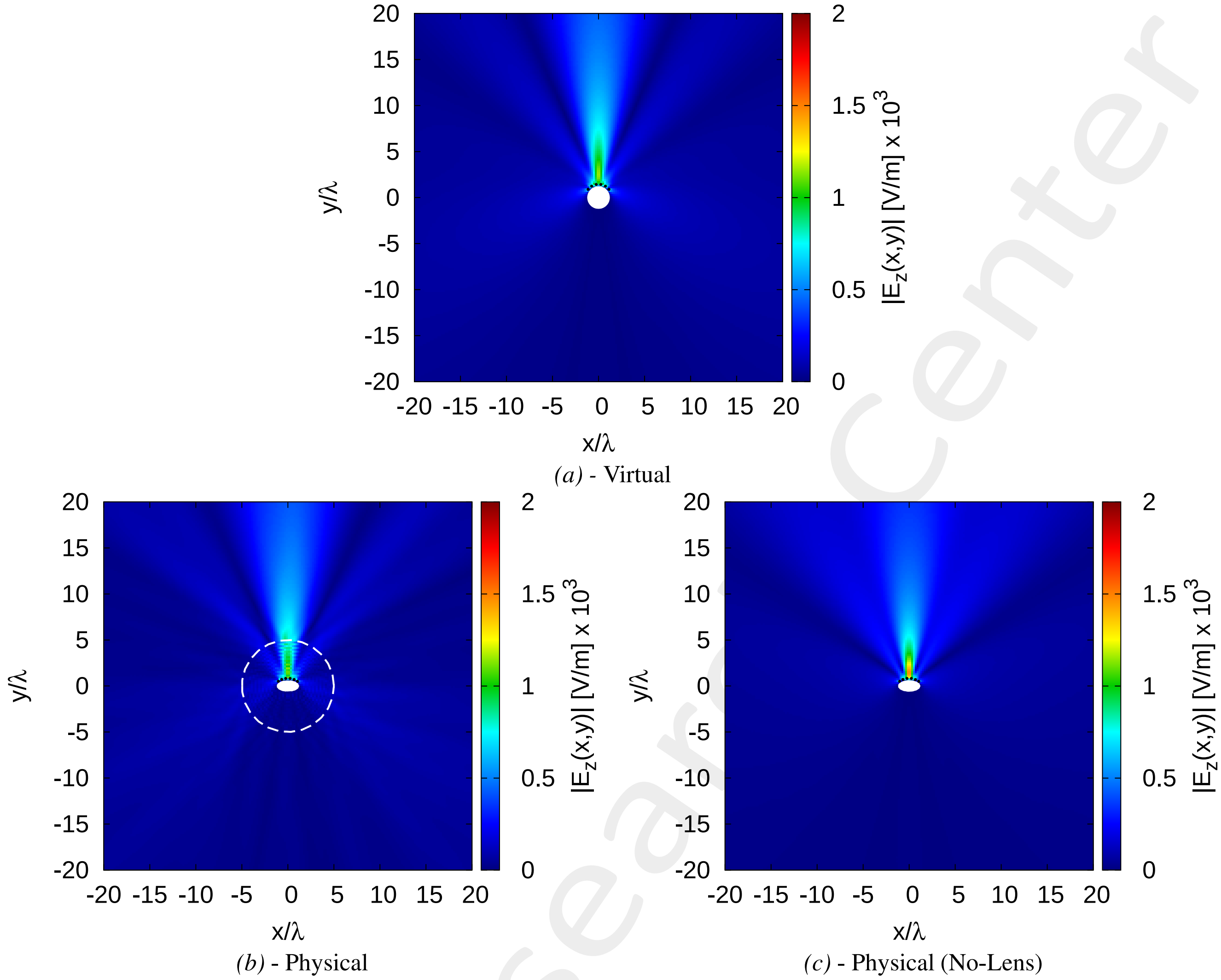

(a) - Virtual

(b) - Physical

(c) - Physical (No-Lens)

Figure 19: Near-Field pattern in the *(a)* virtual, *(b)* physical and *(c)* no-lens

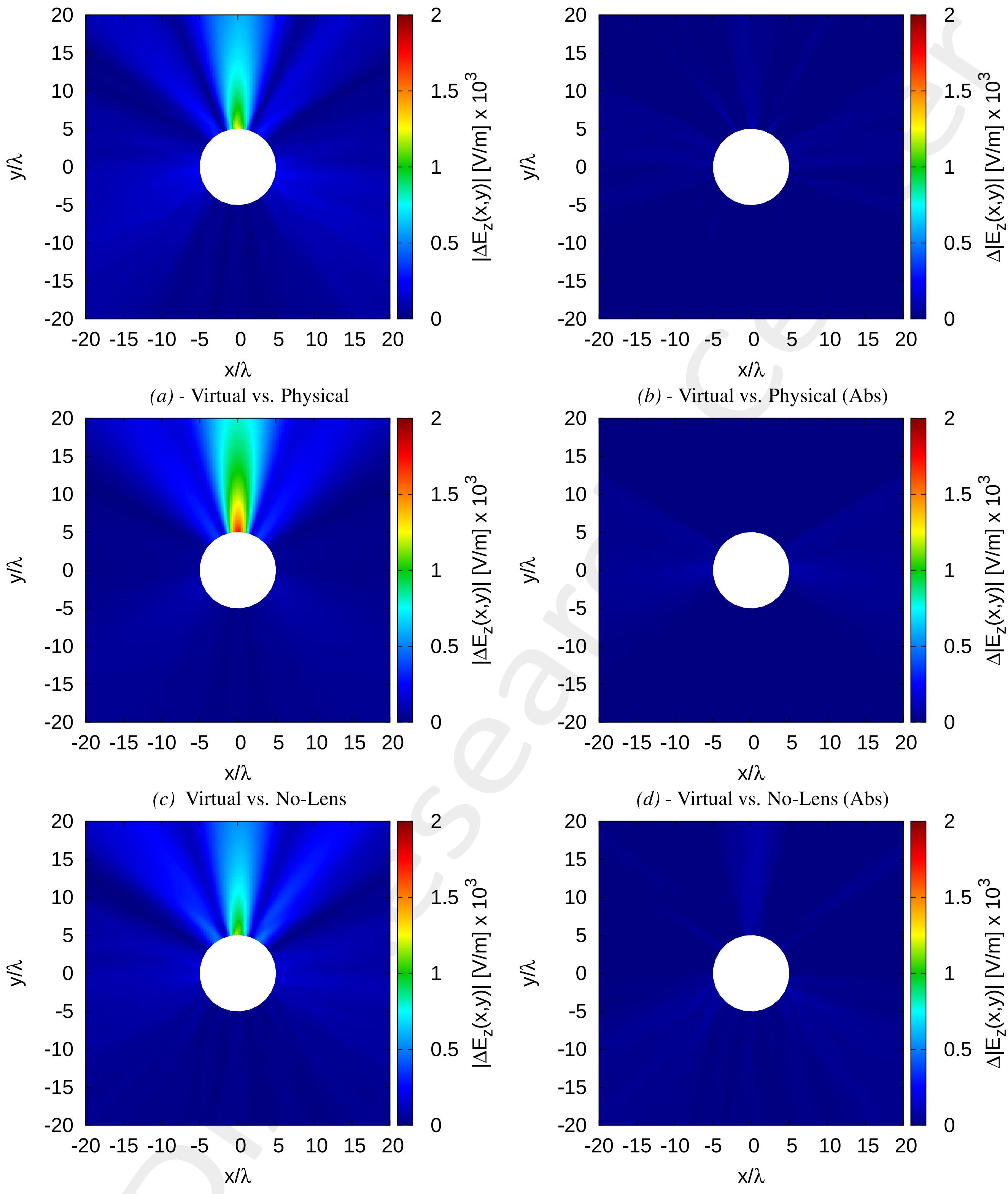

(a) - Virtual vs. Physical

(b) - Virtual vs. Physical (Abs)

(c) Virtual vs. No-Lens

(d) - Virtual vs. No-Lens (Abs)

(e) - Physical vs. No-Lens

(f) - Physical vs. No-Lens (Abs)

Figure 20: Near-Field difference pattern in the *(a)(b)* virtual vs. physical, *(c)(d)* virtual vs. no-lens and *(e)(f)* physical vs. no-lens. The difference pattern is computed for the *(a)(c)(e)* cases as $|\Delta E_z| \triangleq \left|E_z^{ref}(x,y) - E_z^{est}(x,y)\right|_{(x,y)\notin\Omega}$ while for the *(b)(d)(f)* cases as $\Delta|E_z| \triangleq \left[\left|E_z^{ref}(x,y)\right| - \left|E_z^{est}(x,y)\right|\right]_{(x,y)\notin\Omega}$

Deformation $\Psi = 70\%$

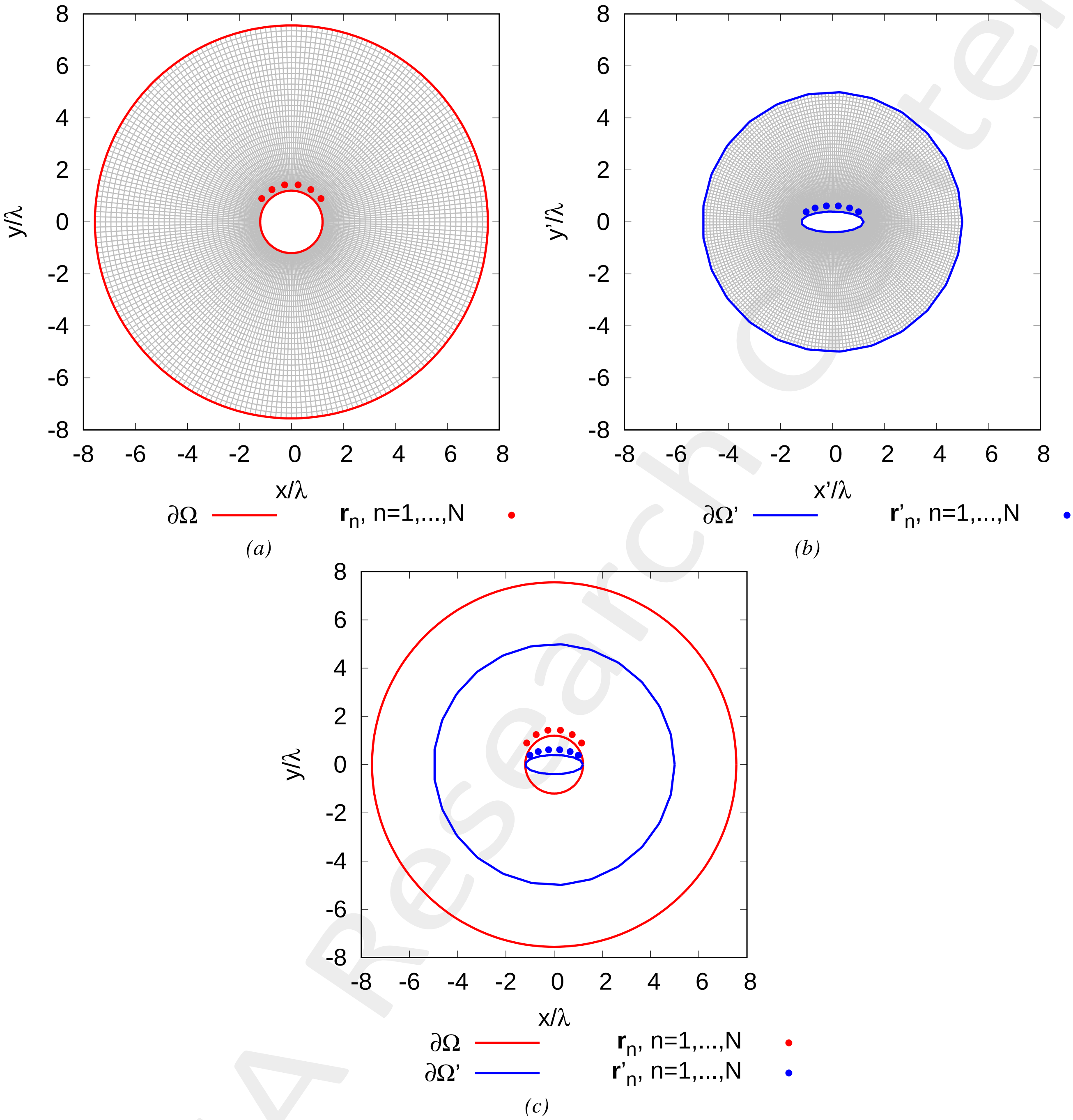

Figure 21: *(a)* Virtual, *(b)* Physical geometries and *(c)* the comparison

Physical Permittivity Properties	
Average fractional anisotropy α_F	0.480449
Average relative anisotropy α_R	0.527215

Table XIII: Average fractional anisotropy α_F and average relative anisotropy α_R

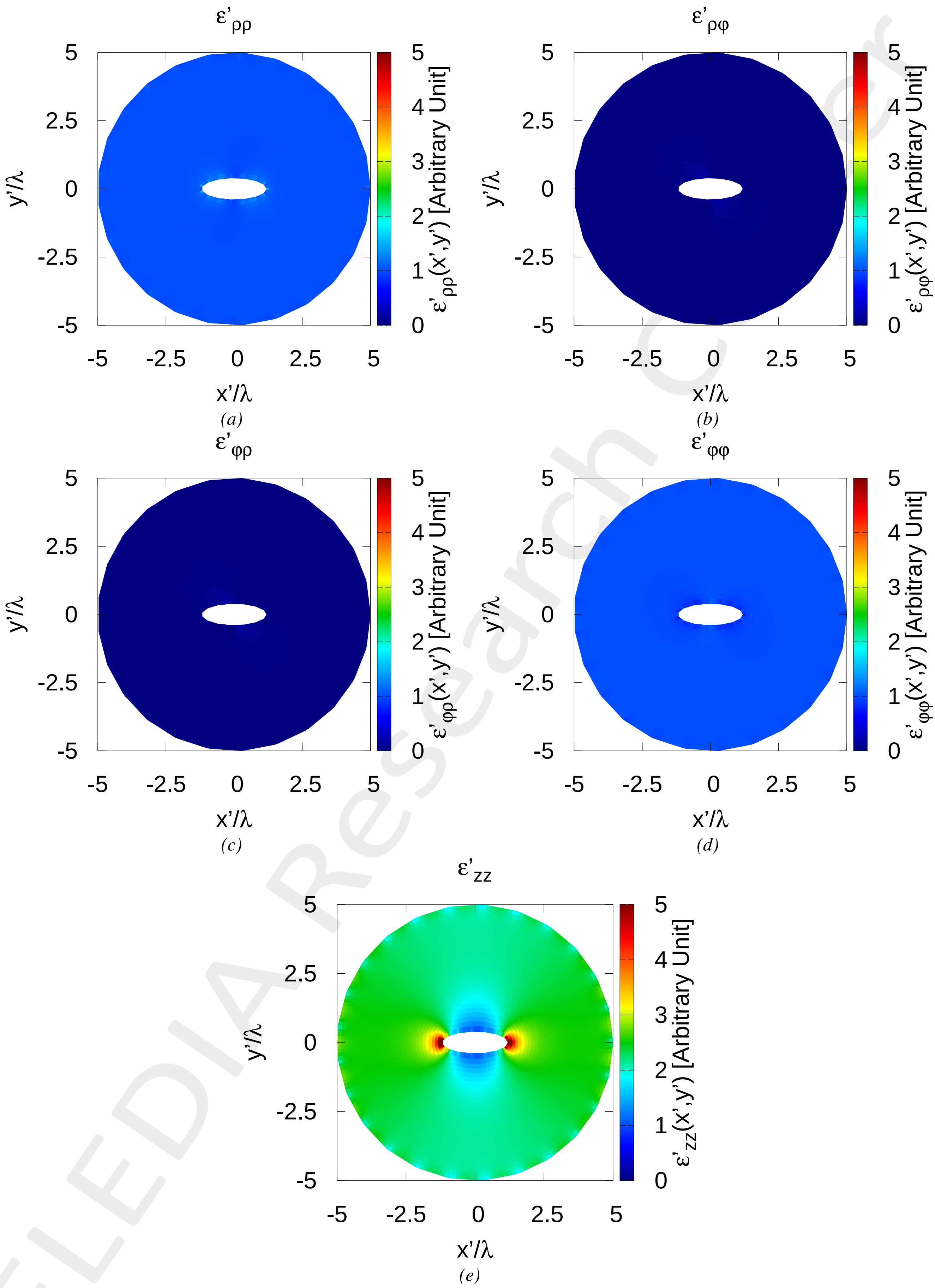

Figure 22: Tensor permittivity values for *(a)* $\varepsilon'_{\rho\rho}$, *(b)* $\varepsilon'_{\rho\varphi}$, *(c)* $\varepsilon'_{\varphi\rho}$, *(d)* $\varepsilon'_{\varphi\varphi}$, *(e)* ε'_{zz}

mimimum/maximum	min	max
$\varepsilon'_{\rho\rho}$	9.3291×10^{-1}	2.2991
$\varepsilon'_{\rho\varphi}$	-5.0291×10^{-1}	3.3914×10^{-1}
$\varepsilon'_{\varphi\rho}$	-5.0291×10^{-1}	3.3914×10^{-1}
$\varepsilon'_{\varphi\varphi}$	4.5820×10^{-1}	1.0719
ε'_{zz}	1.0349	21.6806
global minimum/maximum	$\min\{\underline{\underline{\varepsilon}}'\} = -0.5$	$\max\{\underline{\underline{\varepsilon}}'\} = 21.68$

Table XIV: Statistics about the permittivity lens reporting minimum and maximum value for every component of $\underline{\underline{\varepsilon}}'$, global minimum $\min\{\underline{\underline{\varepsilon}}'\}$ and global maximum $\max\{\underline{\underline{\varepsilon}}'\}$

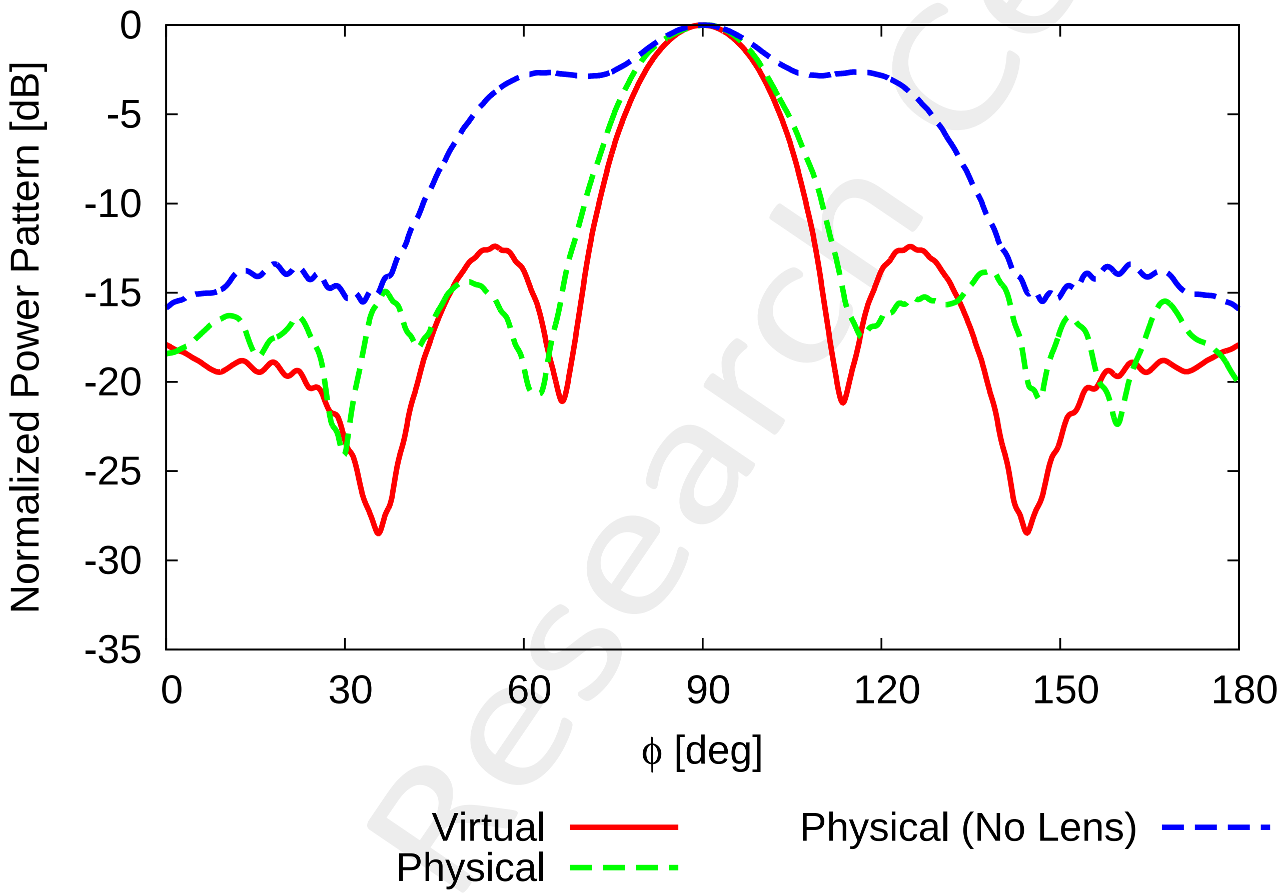

Figure 23: Far-Field Pattern for $\theta = 90$ [deg] and $\varphi \in [0, 180]$ [deg]

	Virtual	Physical	Physical (No Lens)
SLL [dB]	-12.40	-13.76	-2.6305
Directivity [dB]	8.82	8.28	5.23
FNBW [deg]	47.09	54.20	39.79
HPBW [deg]	20.54	23.13	62.61
Field Matching Error ξ (7)	$\times$	3.2930×10^{-2}	2.2826×10^{-1}
Field Matching Error χ (8)	$\times$	3.9125	2.4260

Table XV: Pattern values for the virtual, physical and physical (no lens) cases

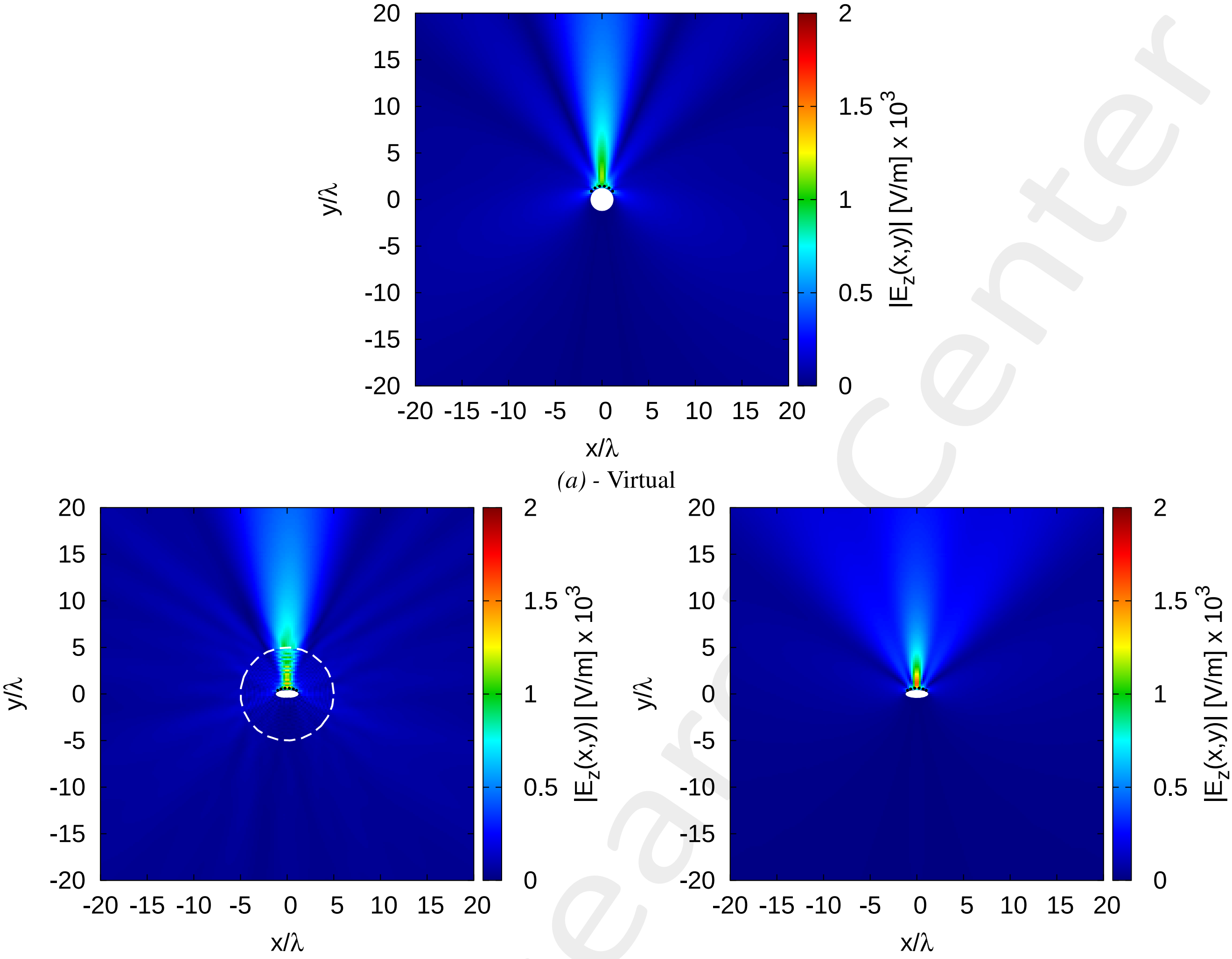

(a) - Virtual

(b) - Physical

(c) - Physical (No-Lens)

Figure 24: Near-Field pattern in the *(a)* virtual, *(b)* physical and *(c)* no-lens

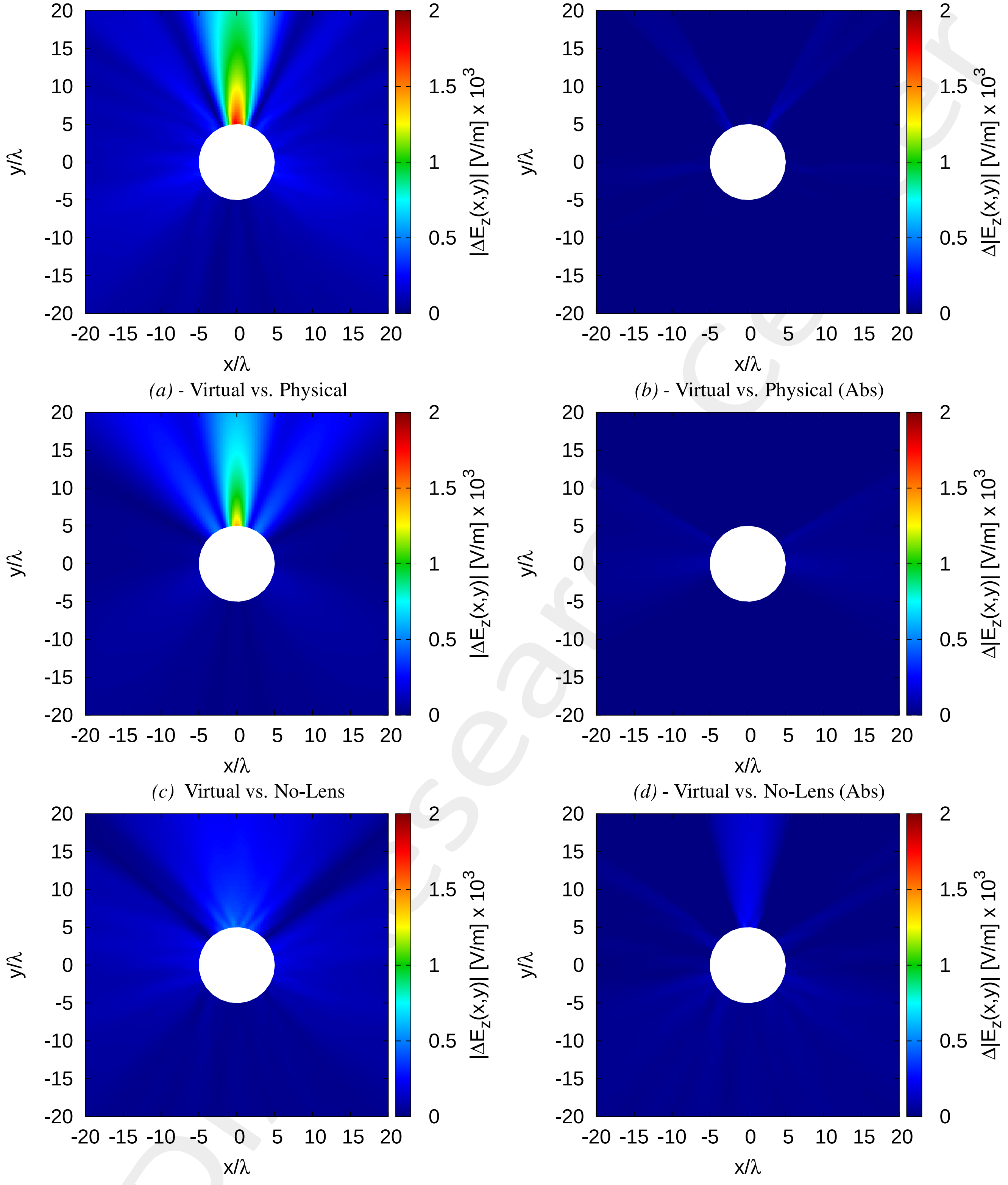

(a) - Virtual vs. Physical

(b) - Virtual vs. Physical (Abs)

(c) Virtual vs. No-Lens

(d) - Virtual vs. No-Lens (Abs)

(e) - Physical vs. No-Lens

(f) - Physical vs. No-Lens (Abs)

Figure 25: Near-Field difference pattern in the *(a)(b)* virtual vs. physical, *(c)(d)* virtual vs. no-lens and *(e)(f)* physical vs. no-lens. The difference pattern is computed for the *(a)(c)(e)* cases as $|\Delta E_z| \triangleq \left|E_z^{ref}(x,y) - E_z^{est}(x,y)\right|_{(x,y)\notin\Omega}$ while for the *(b)(d)(f)* cases as $\Delta|E_z| \triangleq \left[\left|E_z^{ref}(x,y)\right| - \left|E_z^{est}(x,y)\right|\right]_{(x,y)\notin\Omega}$

Deformation $\Psi = 90\%$

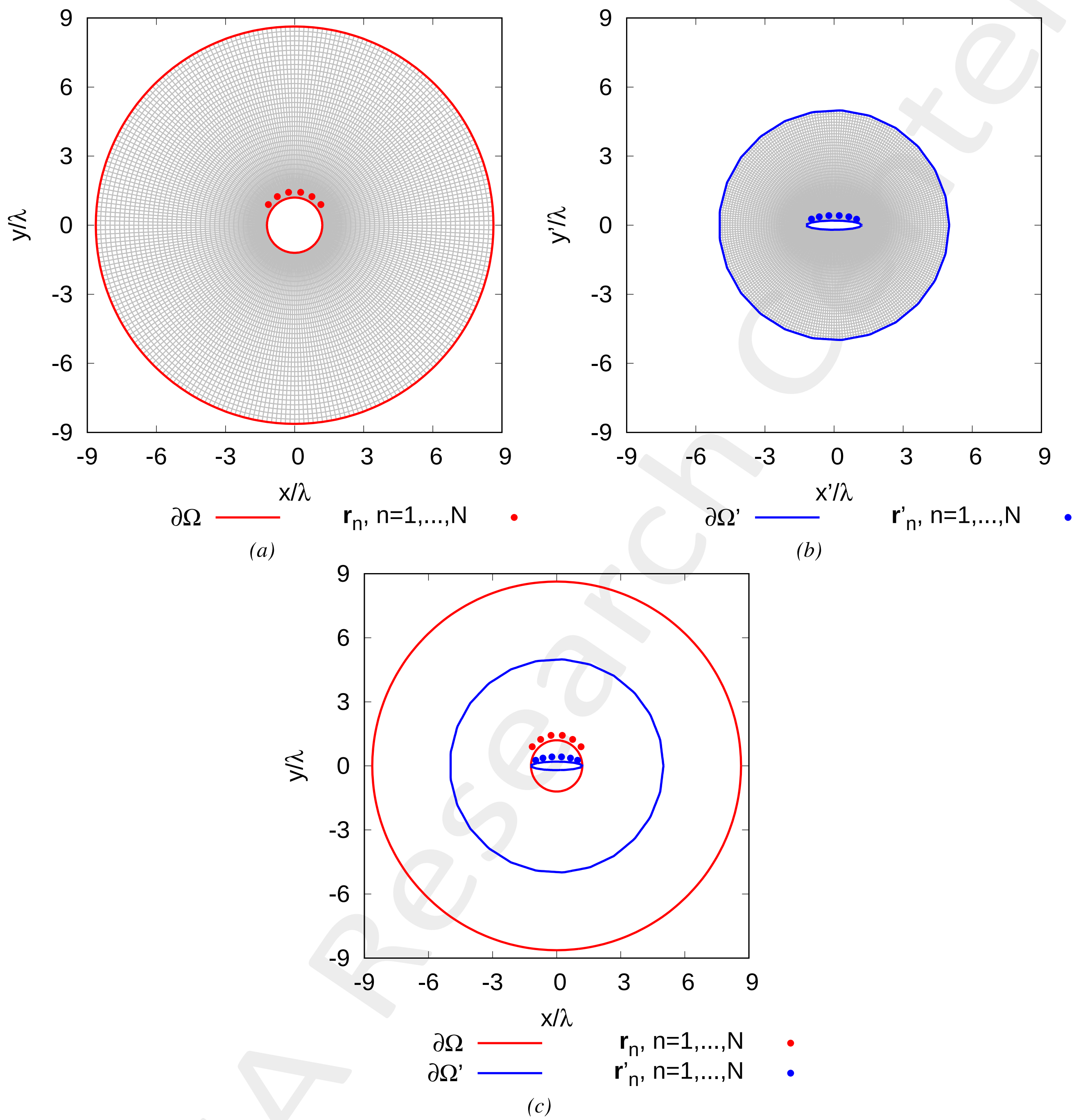

Figure 26: *(a)* Virtual, *(b)* Physical geometries and *(c)* the comparison

Physical Permittivity Properties	
Average fractional anisotropy α_F	0.59743
Average relative anisotropy α_R	0.755638

Table XVI: Average fractional anisotropy α_F and average relative anisotropy α_R

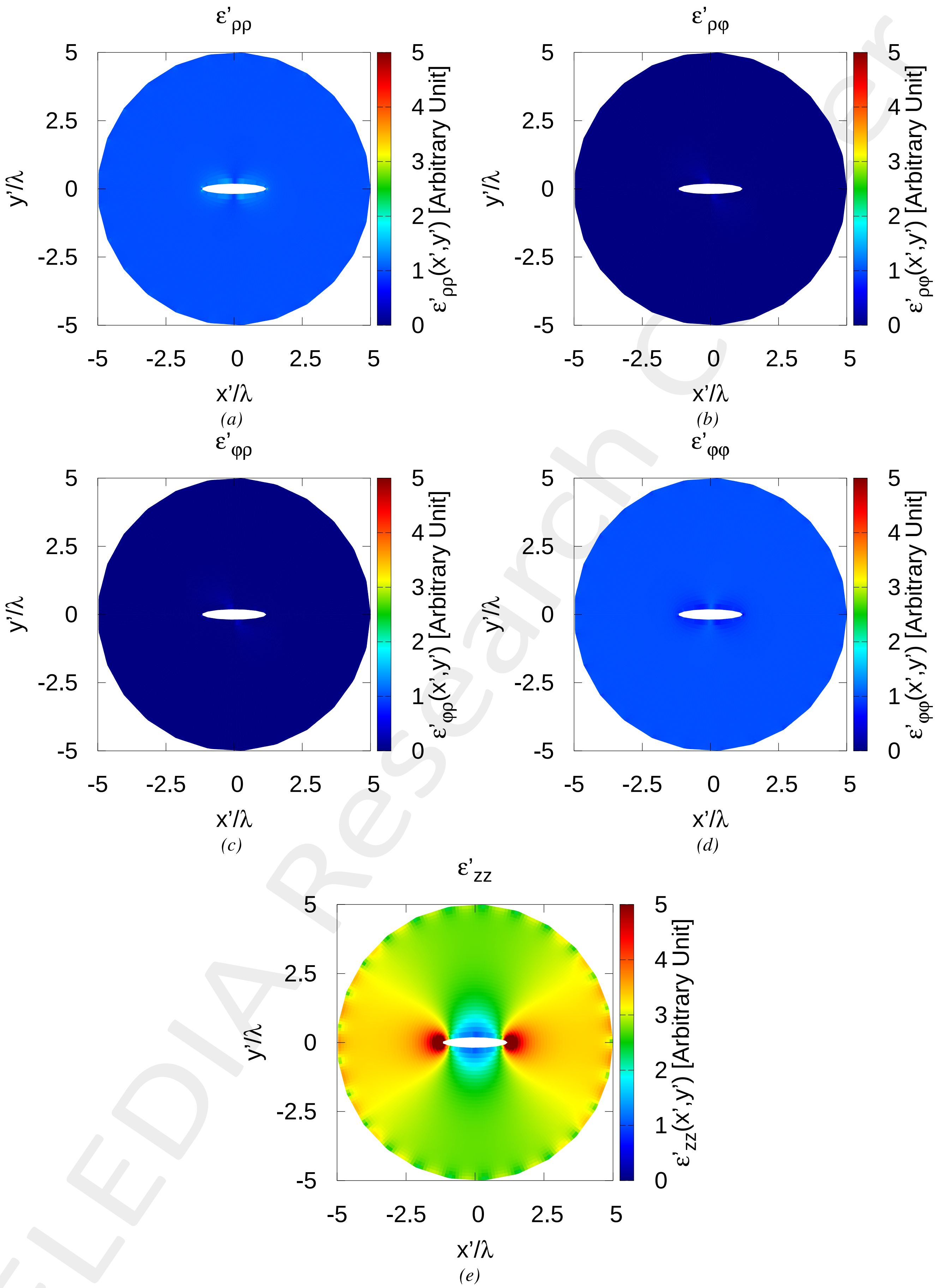

Figure 27: Tensor permittivity values for *(a)* $\varepsilon'_{\rho\rho}$, *(b)* $\varepsilon'_{\rho\varphi}$, *(c)* $\varepsilon'_{\varphi\rho}$, *(d)* $\varepsilon'_{\varphi\varphi}$, *(e)* ε'_{zz}

mimimum/maximum	min	max
$\varepsilon'_{\rho\rho}$	9.2639×10^{-1}	4.9129
$\varepsilon'_{\rho\varphi}$	-9.9273×10^{-1}	7.1883×10^{-1}
$\varepsilon'_{\varphi\rho}$	-9.9273×10^{-1}	7.1883×10^{-1}
$\varepsilon'_{\varphi\varphi}$	2.1943×10^{-1}	1.1192
ε'_{zz}	1.0682	1.4825×10^{2}
global minimum/maximum	$\min\{\underline{\underline{\varepsilon}}'\} = -0.99$	$\max\{\underline{\underline{\varepsilon}}'\} = 148.25$

Table XVII: Statistics about the permittivity lens reporting minimum and maximum value for every component of $\underline{\underline{\varepsilon}}'$, global minimum $\min\{\underline{\underline{\varepsilon}}'\}$ and global maximum $\max\{\underline{\underline{\varepsilon}}'\}$

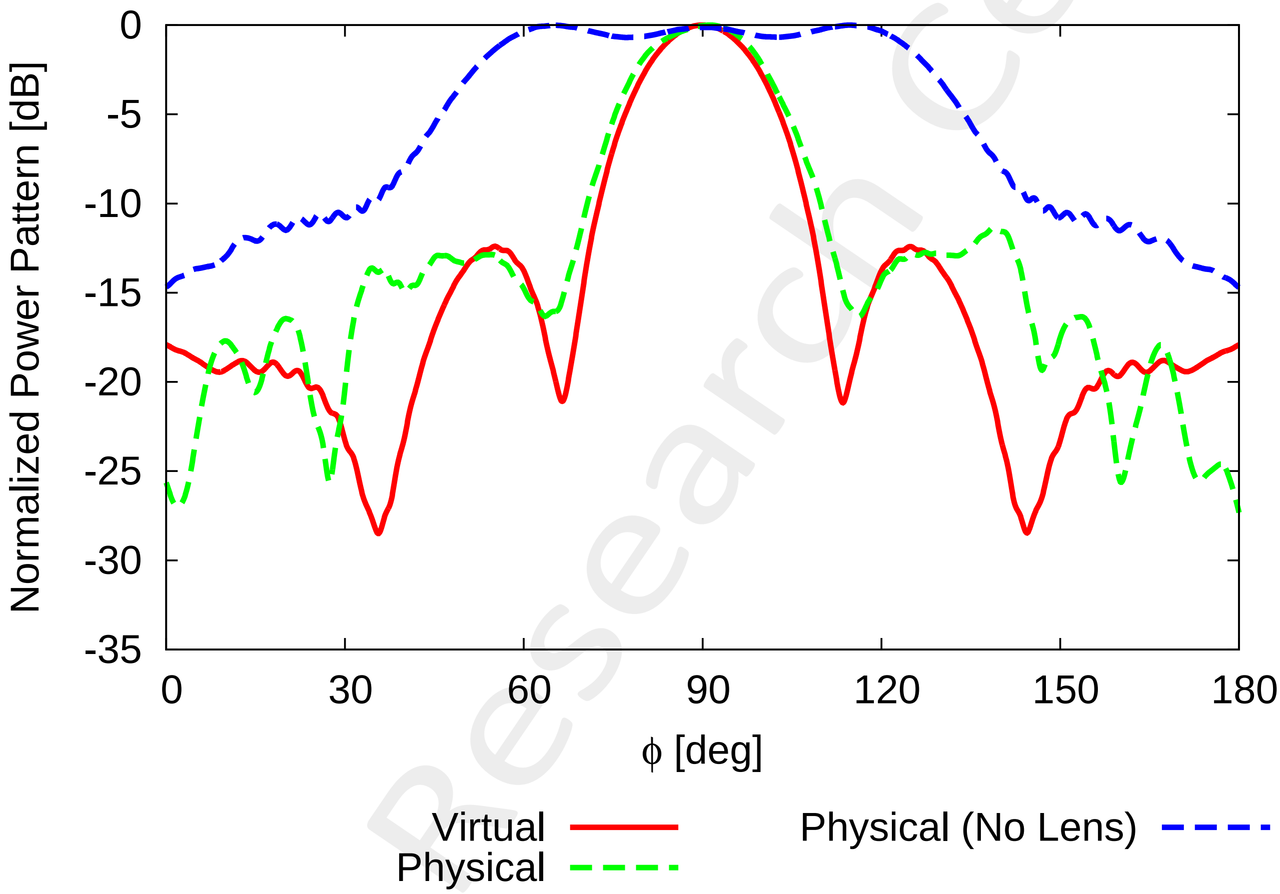

Figure 28: Far-Field Pattern for $\theta = 90$ [deg] and $\varphi \in [0, 180]$ [deg]

	Virtual	Physical	Physical (No Lens)
SLL [dB]	-12.40	-11.35	-1.17×10^{-2}
Directivity [dB]	8.82	8.14	3.42
FNBW [deg]	47.09	52.67	39.79
HPBW [deg]	20.54	23.28	79.08
Field Matching Error ξ (7)	$\times$	3.2251×10^{-2}	3.4788×10^{-1}
Field Matching Error χ (8)	$\times$	2.9344	1.3338

Table XVIII: Pattern values for the virtual, physical and physical (no lens) cases

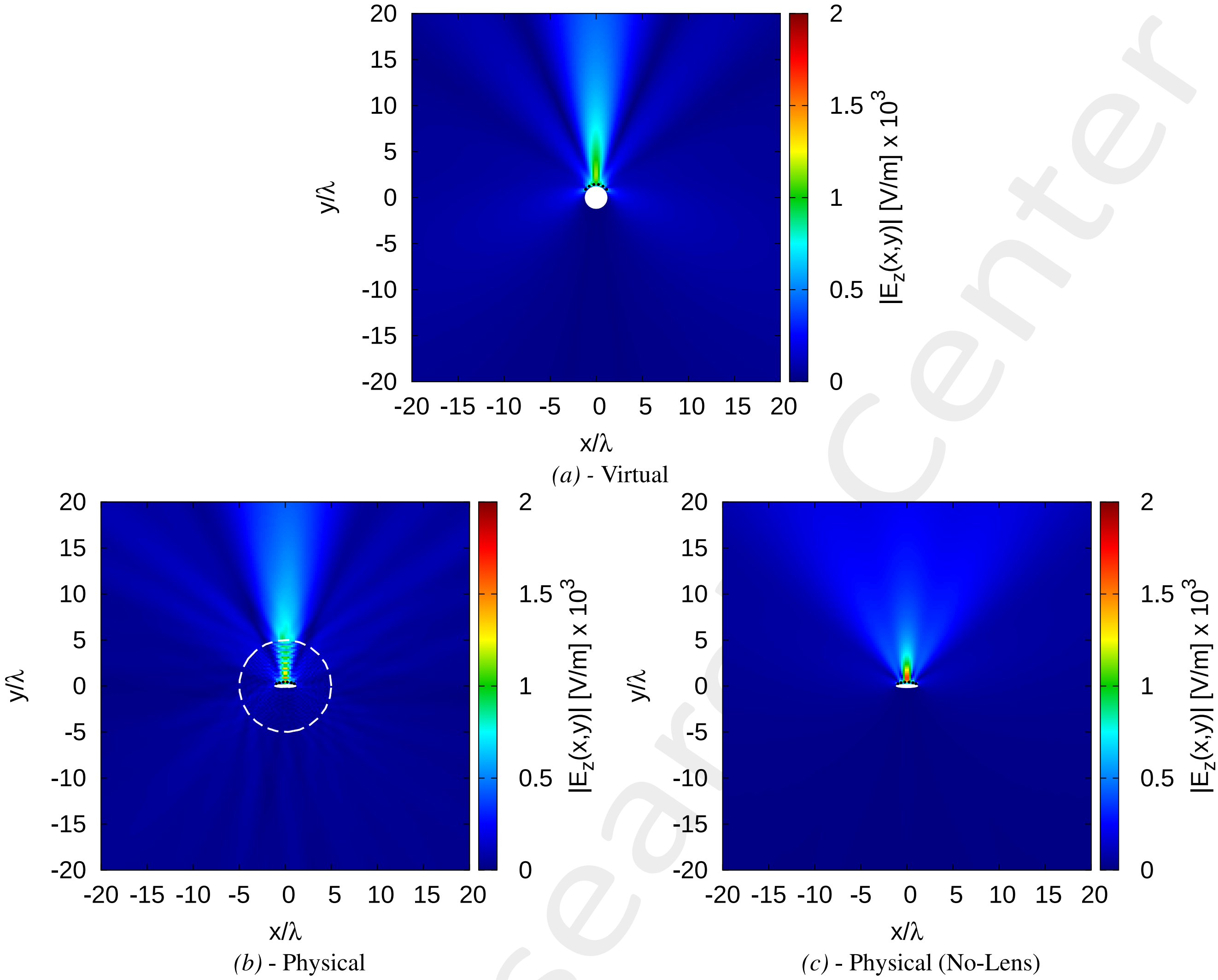

(a) - Virtual

(b) - Physical

(c) - Physical (No-Lens)

Figure 29: Near-Field pattern in the *(a)* virtual, *(b)* physical and *(c)* no-lens

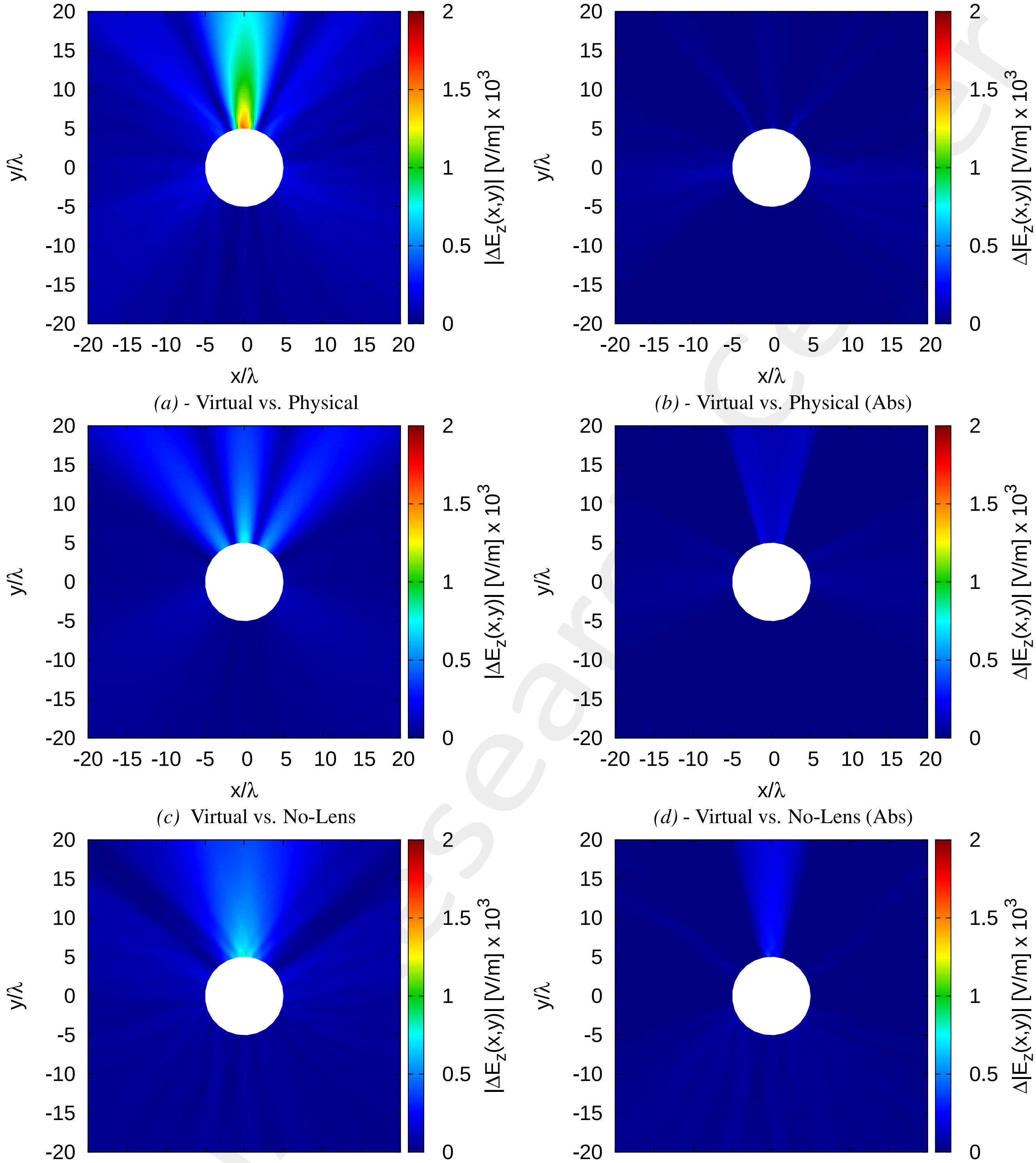

(a) - Virtual vs. Physical

(b) - Virtual vs. Physical (Abs)

(c) Virtual vs. No-Lens

(d) - Virtual vs. No-Lens (Abs)

(e) - Physical vs. No-Lens

(f) - Physical vs. No-Lens (Abs)

Figure 30: Near-Field difference pattern in the *(a)(b)* virtual vs. physical, *(c)(d)* virtual vs. no-lens and *(e)(f)* physical vs. no-lens. The difference pattern is computed for the *(a)(c)(e)* cases as $|\Delta E_z| \triangleq \left|E_z^{ref}(x,y) - E_z^{est}(x,y)\right|_{(x,y)\notin\Omega}$ while for the *(b)(d)(f)* cases as $\Delta|E_z| \triangleq \left[\left|E_z^{ref}(x,y)\right| - \left|E_z^{est}(x,y)\right|\right]_{(x,y)\notin\Omega}$

Deformation $\Psi = 100\%$

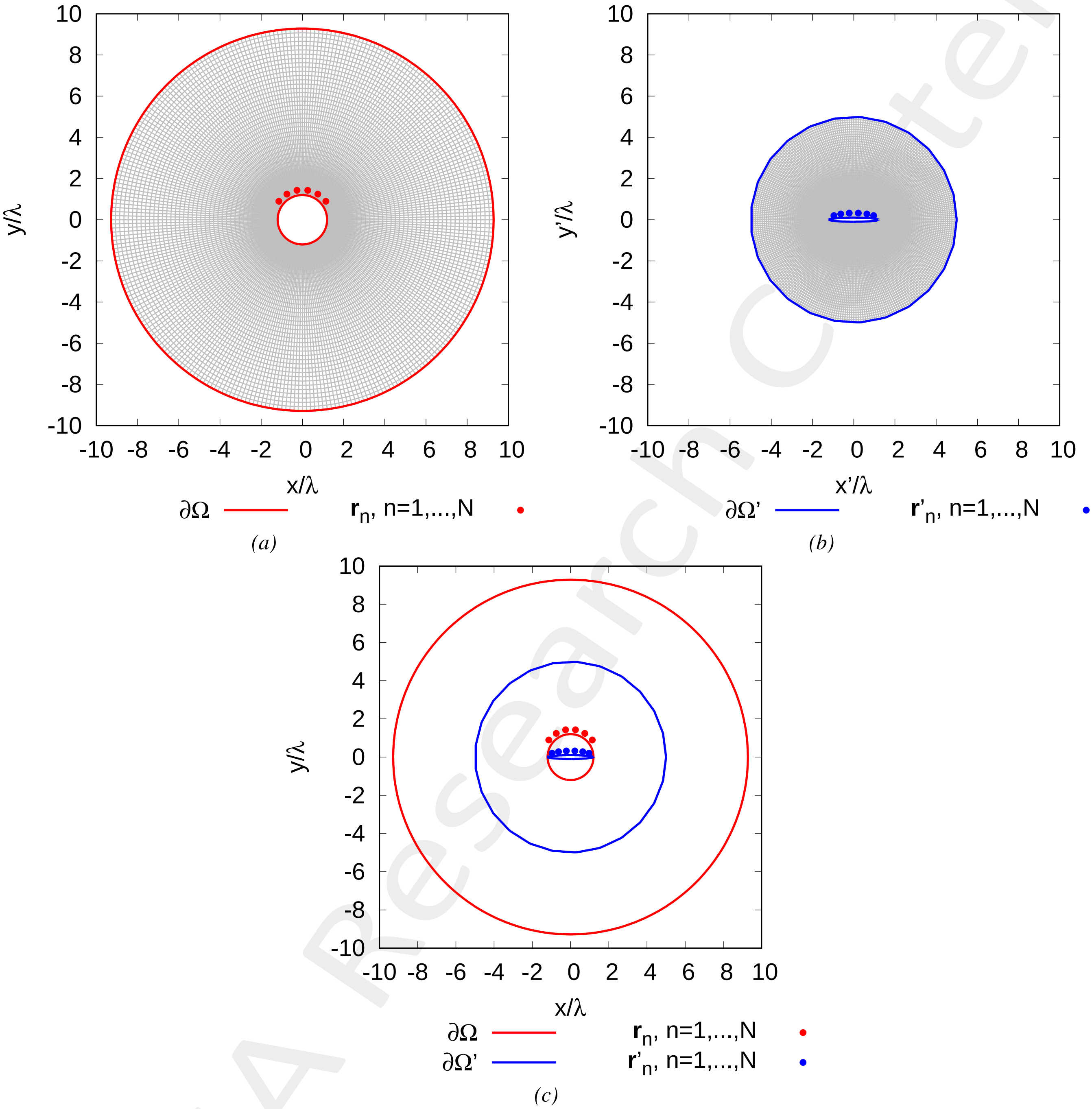

Figure 31: *(a)* Virtual, *(b)* Physical geometries and *(c)* the comparison

Physical Permittivity Properties	
Average fractional anisotropy α_F	0.651728
Average relative anisotropy α_R	0.898396

Table XIX: Average fractional anisotropy α_F and average relative anisotropy α_R

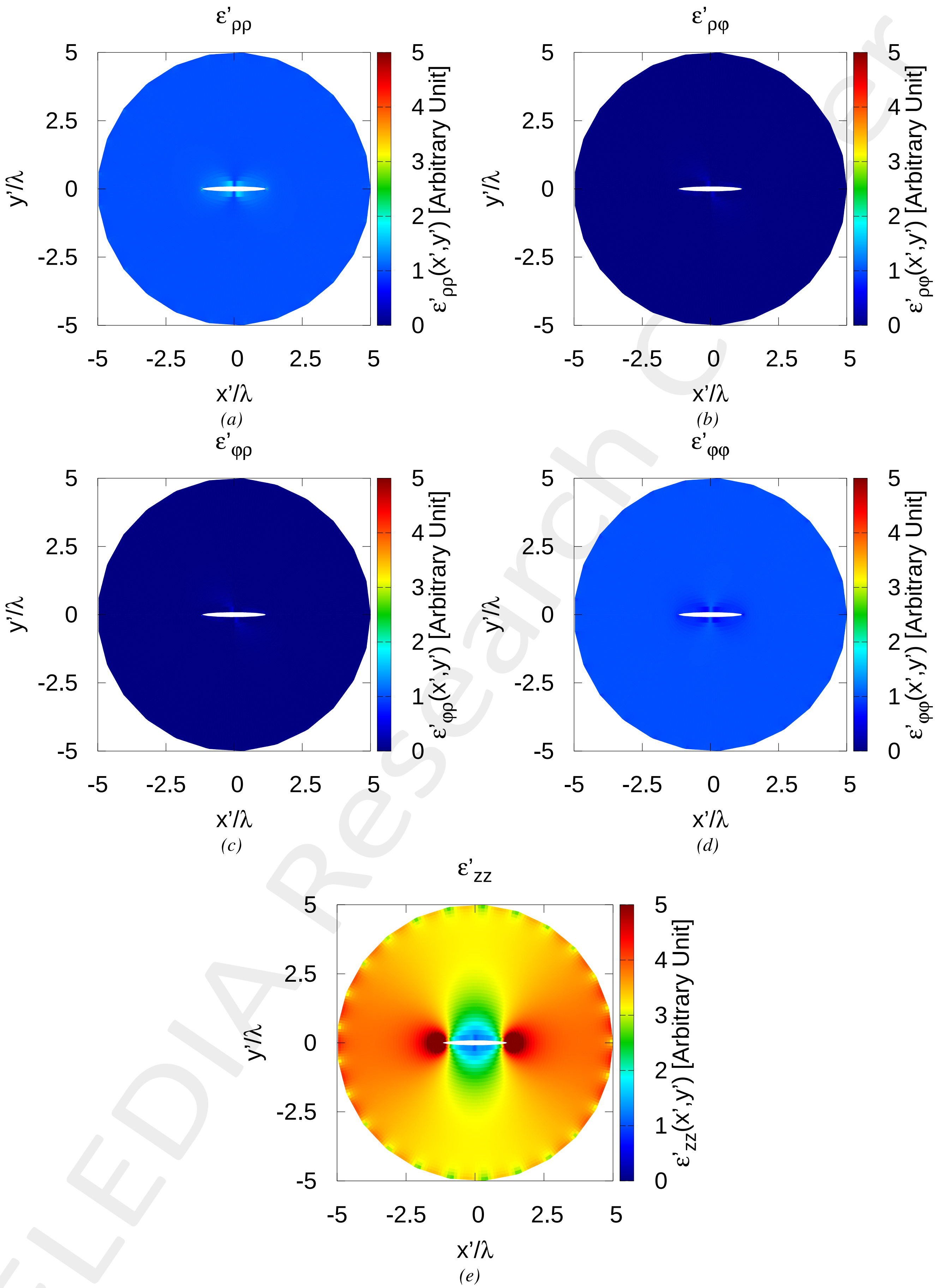

Figure 32: Tensor permittivity values for *(a)* $\varepsilon'_{\rho\rho}$, *(b)* $\varepsilon'_{\rho\varphi}$, *(c)* $\varepsilon'_{\varphi\rho}$, *(d)* $\varepsilon'_{\varphi\varphi}$, *(e)* ε'_{zz}

mimimum/maximum	min	max
$\varepsilon'_{\rho\rho}$	9.1559×10^{-1}	12.1532
$\varepsilon'_{\rho\varphi}$	-1.5426	1.1772
$\varepsilon'_{\varphi\rho}$	-1.5426	1.1772
$\varepsilon'_{\varphi\varphi}$	8.6261×10^{-2}	1.2256
ε'_{zz}	1.0752	8.4165×10^{2}
global minimum/maximum	$\min\{\underline{\underline{\varepsilon}}'\} = -1.54$	$\max\{\underline{\underline{\varepsilon}}'\} = 841.66$

Table XX: Statistics about the permittivity lens reporting minimum and maximum value for every component of $\underline{\underline{\varepsilon}}'$, global minimum $\min\{\underline{\underline{\varepsilon}}'\}$ and global maximum $\max\{\underline{\underline{\varepsilon}}'\}$

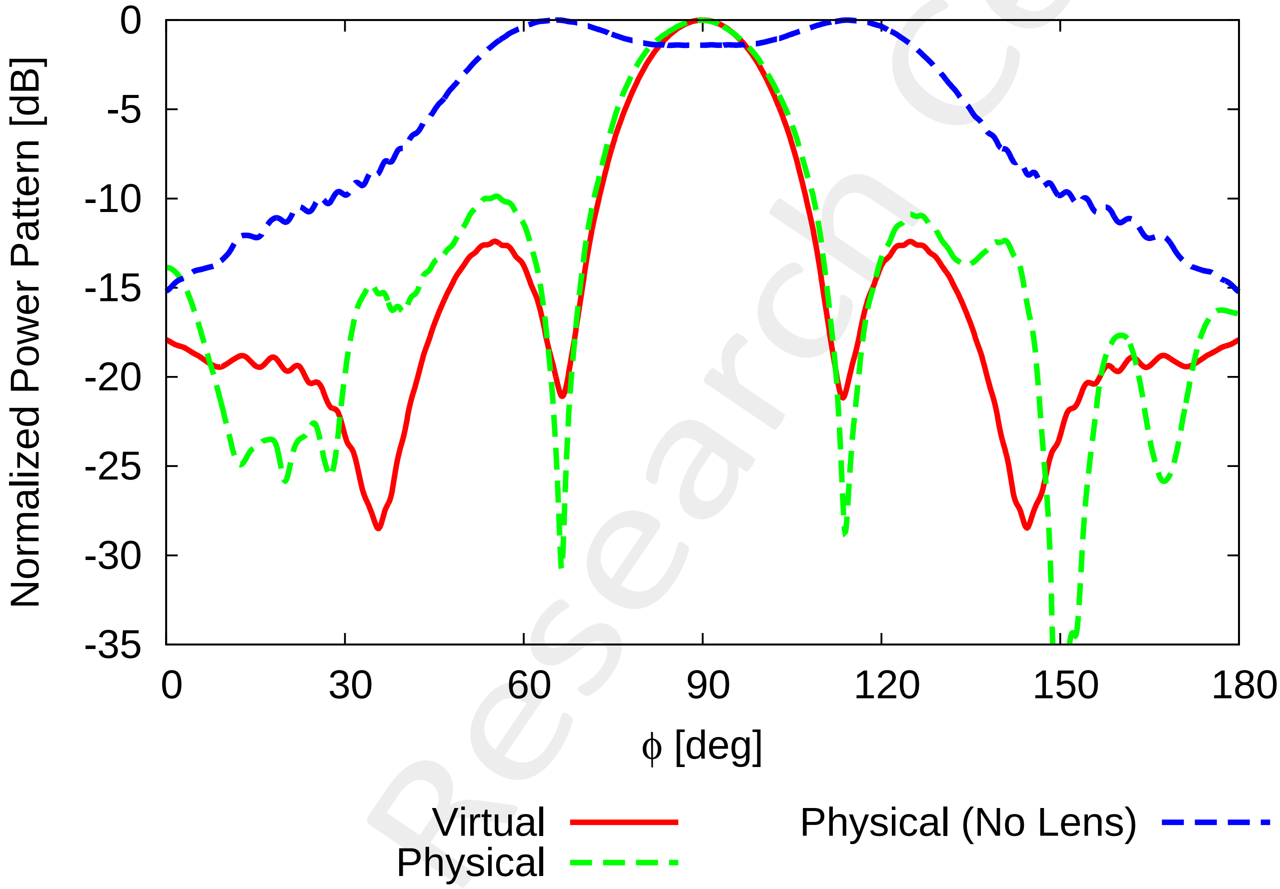

Figure 33: Far-Field Pattern for $\theta = 90$ [deg] and $\varphi \in [0, 180]$ [deg]

	Virtual	Physical	Physical (No Lens)
SLL [dB]	-12.40	-9.87	-1.2663×10^{-3}
Directivity [dB]	8.82	8.27	3.60
FNBW [deg]	47.09	47.54	46.82
HPBW [deg]	20.54	22.65	80.05
Field Matching Error ξ (7)	$\times$	3.0079×10^{-2}	4.0580×10^{-1}
Field Matching Error χ (8)	$\times$	2.3199	1.0882

Table XXI: Pattern values for the virtual, physical and physical (no lens) cases

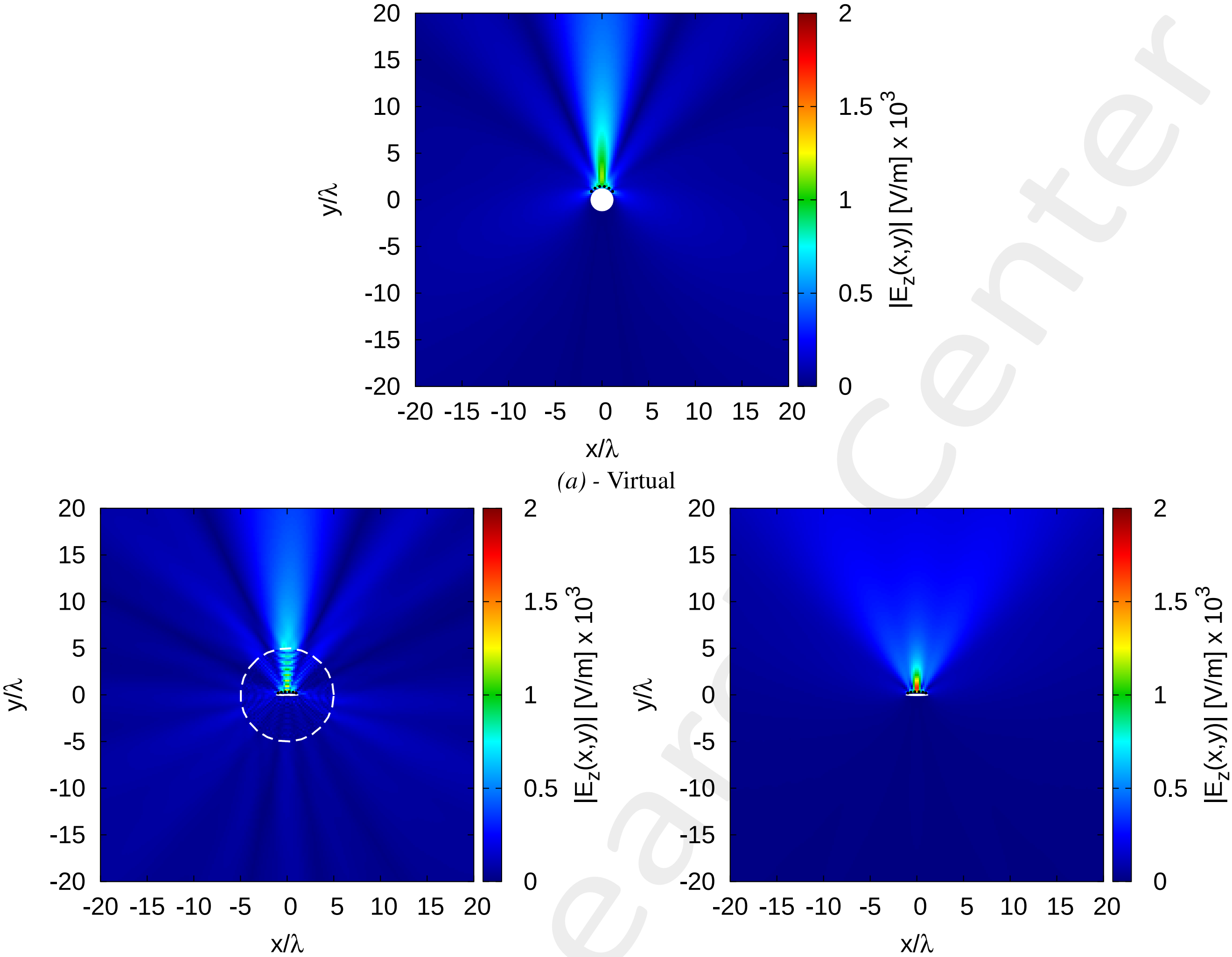

(a) - Virtual

(b) - Physical

(c) - Physical (No-Lens)

Figure 34: Near-Field pattern in the *(a)* virtual, *(b)* physical and *(c)* no-lens

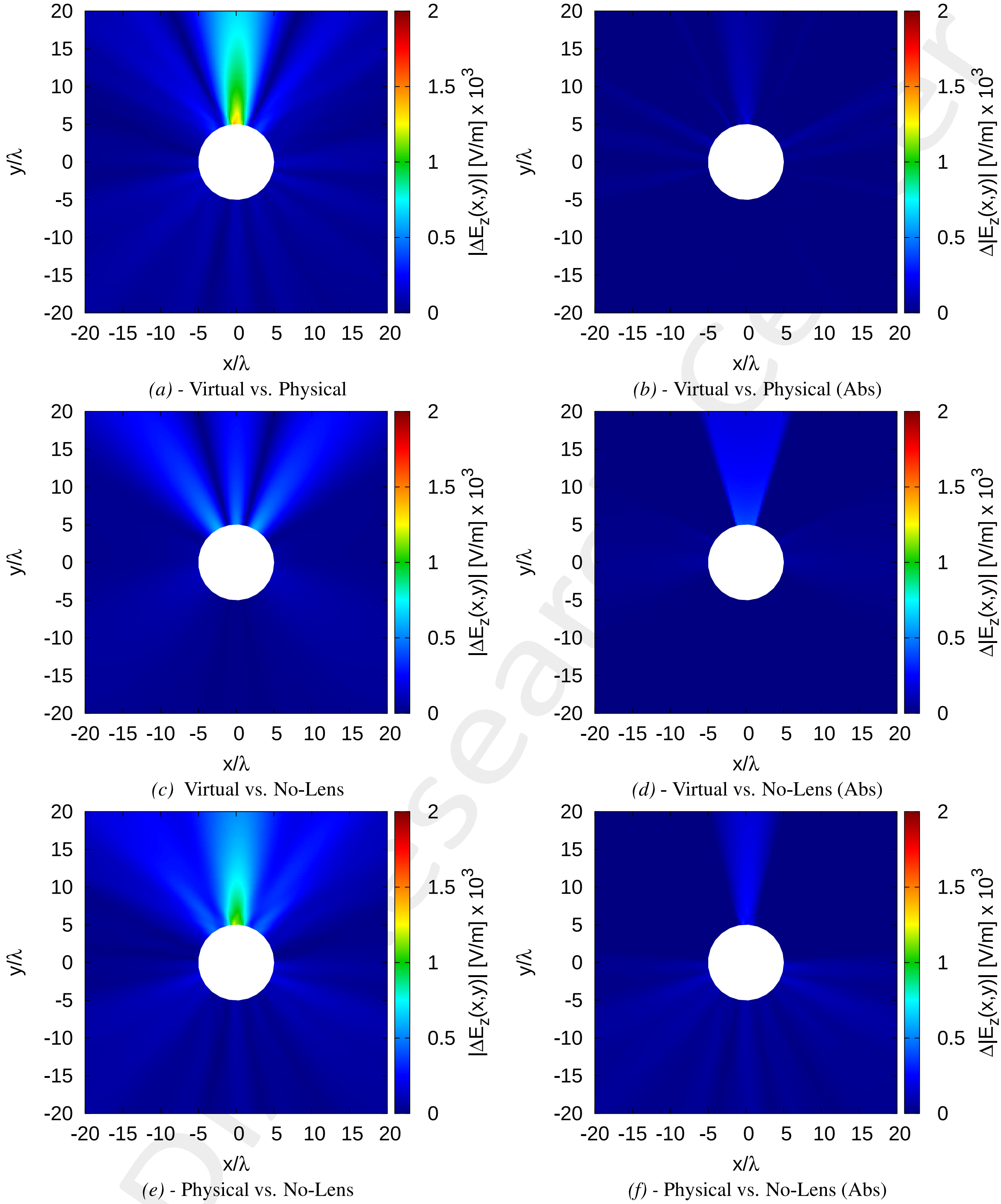

(a) - Virtual vs. Physical

(b) - Virtual vs. Physical (Abs)

(c) Virtual vs. No-Lens

(d) - Virtual vs. No-Lens (Abs)

(e) - Physical vs. No-Lens

(f) - Physical vs. No-Lens (Abs)

Figure 35: Near-Field difference pattern in the *(a)(b)* virtual vs. physical, *(c)(d)* virtual vs. no-lens and *(e)(f)* physical vs. no-lens. The difference pattern is computed for the *(a)(c)(e)* cases as $|\Delta E_z| \triangleq \left|E_z^{ref}(x,y) - E_z^{est}(x,y)\right|_{(x,y)\notin\Omega}$ while for the *(b)(d)(f)* cases as $\Delta|E_z| \triangleq \left[\left|E_z^{ref}(x,y)\right| - \left|E_z^{est}(x,y)\right|\right]_{(x,y)\notin\Omega}$

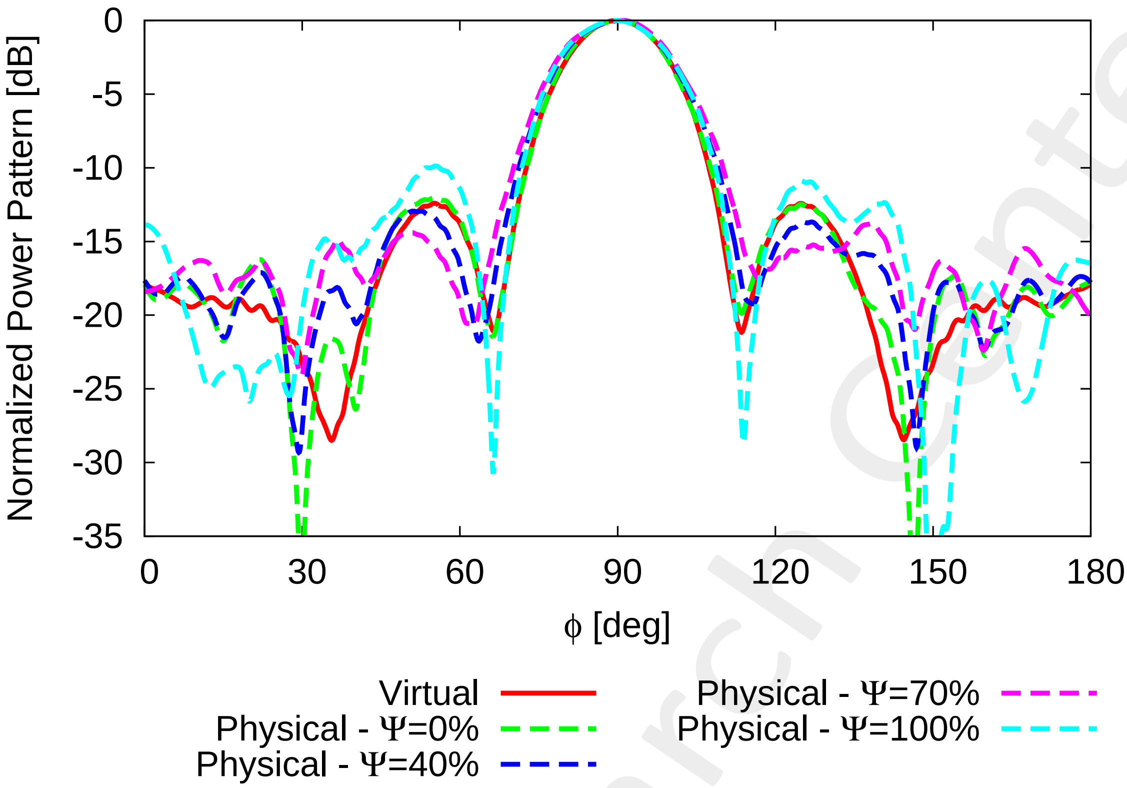

(a)

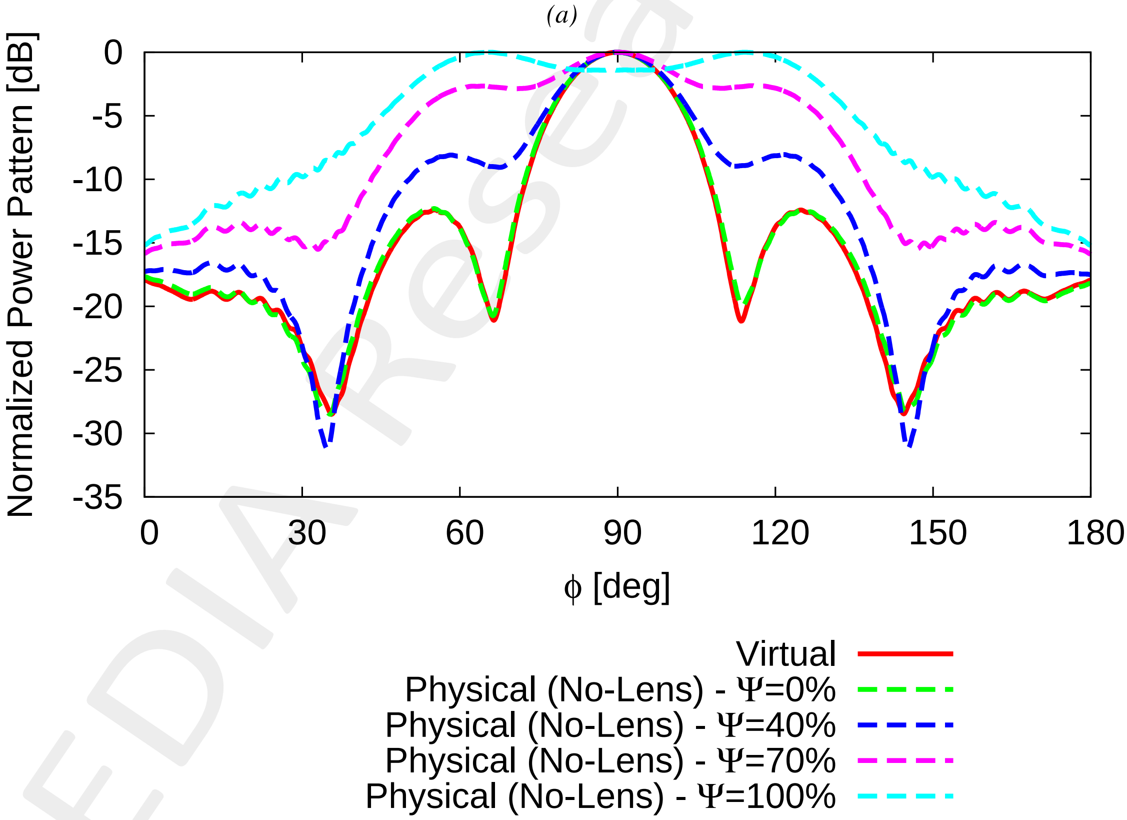

(b)

Figure 36: Far-Field Pattern for $\theta = 90$ [deg] and $\varphi \in [0, 180]$ [deg] at variance of the lens deformation for the *(a)* physical and *(b)* physical (no-lens)

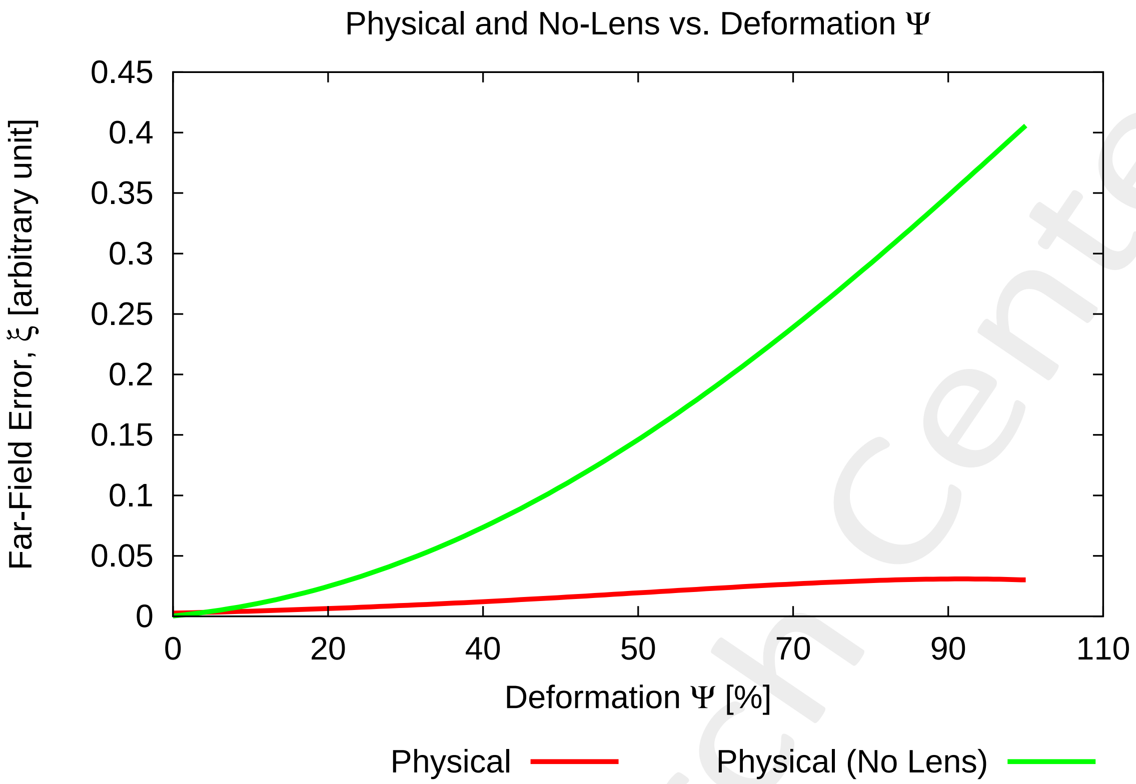

(a)

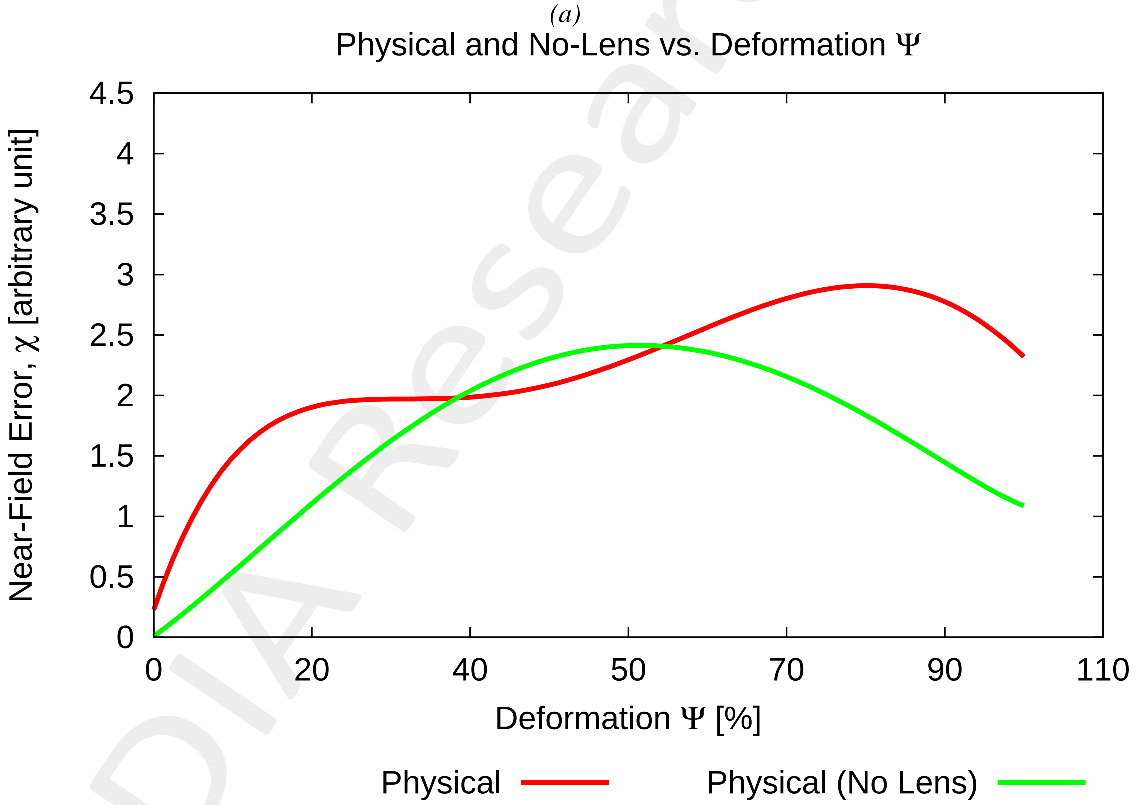

(b)

Figure 37: *(a)* Far-field error ξ and *(b)* near-field error χ for the physical and no-lens cases

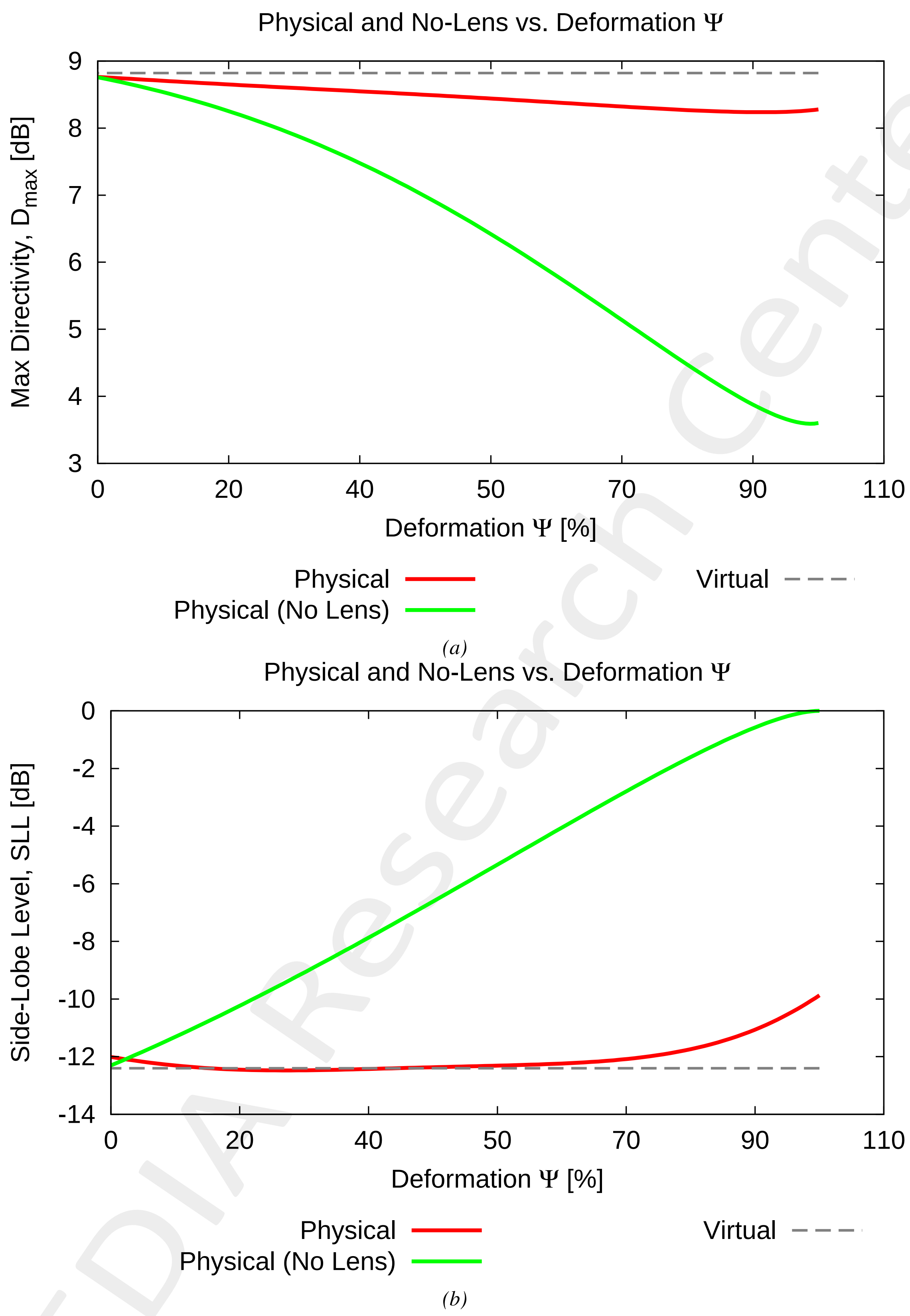

Figure 38: *(a)* Maximum directivity [dB] and *(b)* sidelobe level (SLL) [dB] vs. the deformation degree Ψ

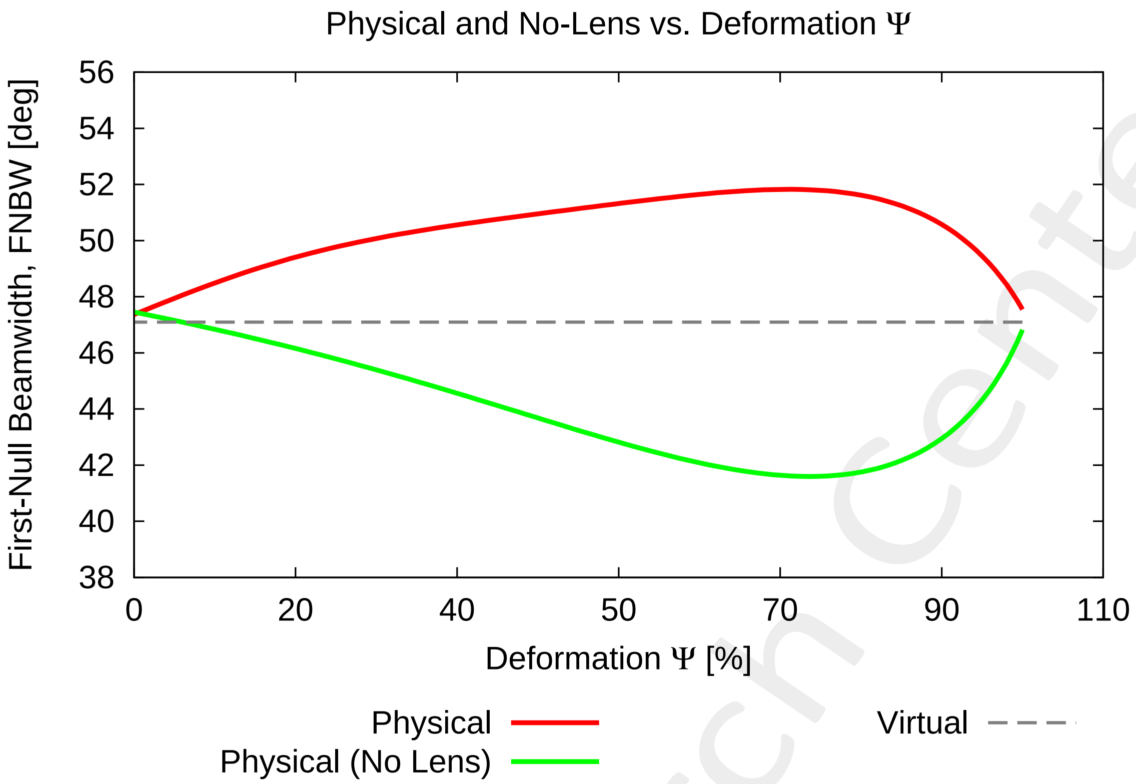

(a)

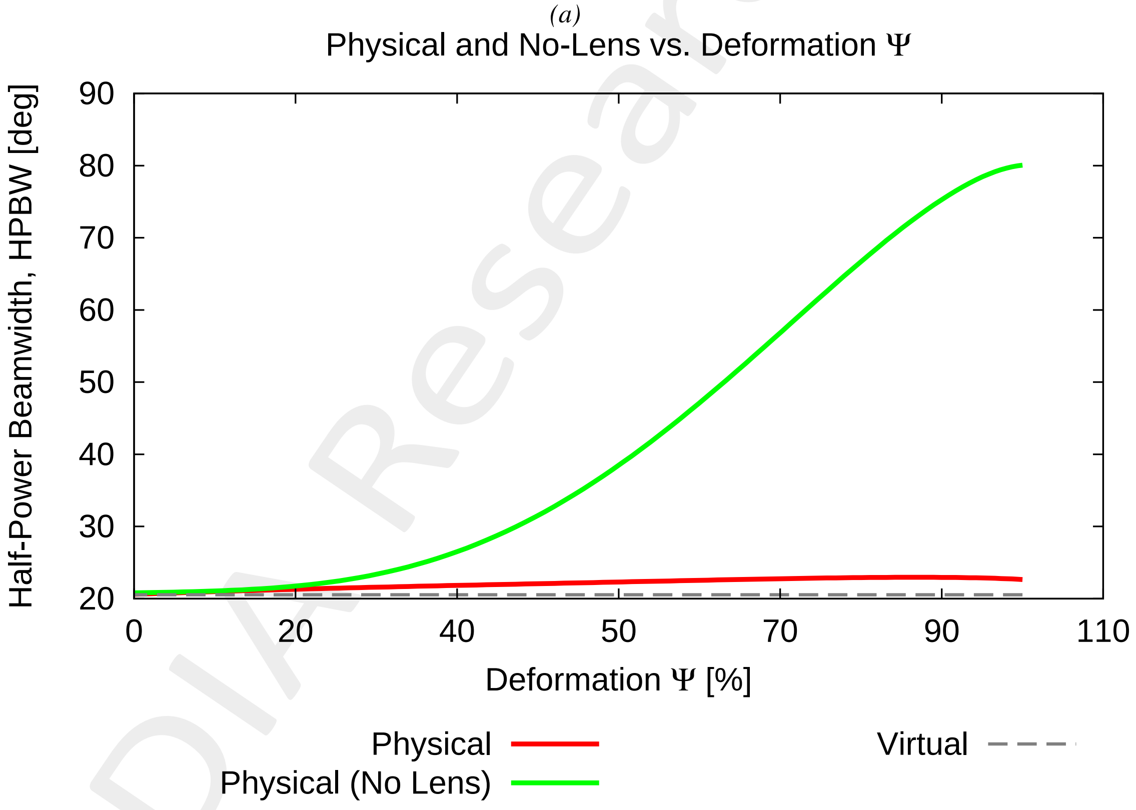

(b)

Figure 39: *(a)* First-null beamwidth (FNBW) [deg] and *(b)* halfpower beamwidth (HPBW) [deg] vs. the deformation degree Ψ

3 Conclusions

An innovative transformation electromagnetics methodology based on the Schwarz-Christoffel theory has been proposed to design conformal phased arrays. The numerical results have shown the effectiveness and the potential of the proposed method.

References

[1] M. Salucci, F. Boulos, A. Polo, and G. Oliveri, “Conformal transformation electromagnetics based on Schwarz-Christoffel mapping for the synthesis of doubly-connected metalenses,” *IEEE Trans. Antennas Propag.*, vol. 68, no. 3, pp. 1836-1850, Mar. 2020.

[2] M. Salucci, L. Tenuti, G. Gottardi, A. Hannan, and A. Massa, "System-by-design method for efficient linear array miniaturisation through low-complexity isotropic lenses" *Electronic Letters*, vol. 55, no. 8, pp. 433-434, May 2019.

[3] M. Salucci, G. Oliveri, N. Anselmi, and A. Massa, "Material-by-design synthesis of conformal miniaturized linear phased arrays," *IEEE Access*, vol. 6, pp. 26367-26382, 2018.

[4] M. Salucci, G. Oliveri, N. Anselmi, G. Gottardi, and A. Massa, "Performance enhancement of linear active electronically-scanned arrays by means of MbD-synthesized metalenses," *Journal of Electromagnetic Waves and Applications*, vol. 32, no. 8, pp. 927-955, 2018.

[5] G. Oliveri, M. Salucci, N. Anselmi and A. Massa, "Multiscale System-by-Design synthesis of printed WAIMs for waveguide array enhancement," *IEEE J. Multiscale Multiphysics Computat. Techn.*, vol. 2, pp. 84-96, 2017.

[6] G. Oliveri, F. Viani, N. Anselmi, and A. Massa, "Synthesis of multi-layer WAIM coatings for planar phased arrays within the system-by-design framework," *IEEE Trans. Antennas Propag.*, vol. 63, no. 6, pp. 2482-2496, June 2015.

[7] A. Massa and G. Oliveri, "Metamaterial-by-Design: Theory, methods, and applications to communications and sensing - Editorial," *EPJ Applied Metamaterials*, vol. 3, no. E1, pp. 1-3, 2016.

[8] G. Oliveri, E. T. Bekele, M. Salucci, and A. Massa, "Transformation electromagnetics miniaturization of sectoral and conical horn antennas," *IEEE Trans. Antennas Propag.*, vol. 64, no. 4, pp. 1508-1513, April 2016.

[9] G. Oliveri, E. T. Bekele, M. Salucci, and A. Massa, "Array miniaturization through QCTO-SI metamaterial radomes" *IEEE Trans. Antennas Propag.*, vol. 63, no. 8, pp. 3465-3476, Aug. 2015.

[10] L. Tenuti, M. Salucci, G. Oliveri, P. Rocca, and A. Massa, “Surrogate- assisted optimization of metamaterial devices for advanced antenna Systems,” Proc. 2015 IEEE Symposium Series on Computational Intelligence (IEEE SSCI 2015), Cape Town, South Africa, pp. 1154-1156, Dec. 8-10, 2015.

[11] G. Oliveri, L. Tenuti, M. Salucci, and A. Massa, “Innovative antenna architectures exploiting metamaterials for new generation radars,” 10th European Conference on Antennas and Propagation (EUCAP 2016), Davos, Switzerland, pp. 1-3, April 11-15, 2016.

[12] M. Salucci, G. Oliveri, H. Ahmadi, and A. Massa, "Conformal transformation of linear arrays through QCTO-based design tools," Proc. 2016 IEEE AP-S International Symposium and USNC-URSI Radio Science Meeting, Fajardo, Puerto Rico, pp. 1083- 1084, July 26 - July 1, 2016.

[13] M. Salucci, L. Tenuti, E. Bekele, and G. Oliveri, "Enhancement of linear arrays through MbD metamaterial coatings," Proc. 2016 IEEE AP-S International Symposium and USNC-URSI Radio Science Meeting, Fajardo, Puerto Rico, pp. 1089- 1090, July 26 - July 1, 2016.

[14] P. Rocca, N. Anselmi, A. Polo, and A. Massa, "An irregular two-sizes square tiling method for the design of isophoric phased arrays," *IEEE Trans. Antennas Propag.*, vol. 68, no. 6, pp. 4437-4449, Jun. 2020.

[15] P. Rocca, N. Anselmi, A. Polo, and A. Massa, "Modular design of hexagonal phased arrays through diamond tiles," *IEEE Trans. Antennas Propag.*, vol.68, no. 5, pp. 3598-3612, May 2020.

[16] N. Anselmi, L. Poli, P. Rocca, and A. Massa, "Design of simplified array layouts for preliminary experimental testing and validation of large AESAs," *IEEE Trans. Antennas Propag.*, vol. 66, no. 12, pp. 6906-6920, Dec. 2018.

[17] N. Anselmi, P. Rocca, M. Salucci, and A. Massa, "Contiguous phase-clustering in multibeam-on-receive scanning arrays" *IEEE Trans. Antennas Propag.*, vol. 66, no. 11, pp. 5879-5891, Nov. 2018.

[18] N. Anselmi, P. Rocca, M. Salucci, and A. Massa, "Irregular phased array tiling by means of analytic schemata-driven optimization," *IEEE Trans. Antennas Propag.*, vol. 65, no. 9, pp. 4495-4510, Sept. 2017.

[19] N. Anselmi, P. Rocca, M. Salucci, and A. Massa, "Optimization of excitation tolerances for robust beamforming in linear arrays" *IET Microwaves, Antennas & Propagation*, vol. 10, no. 2, pp. 208-214, 2016.